PFS on Mars Express: preparing the analysis of infrared spectra to be measured by the Planetary Fourier Spectrometer

R. Haus[a,*], D.V. Titov[b]

[a]*German Aerospace Center (DLR), Institute of Space Sensor Technology and Planetary Exploration, Rutherfordstraße 2, D-12489 Berlin, Germany*
[b]*Max Planck Institute for Aeronomy, Max-Planck-Straße 2, D-37191 Katlenburg-Lindau, Germany*

Abstract

A radiative transfer simulation and retrieval technique (RRT) is described that will be applied to derive atmospheric and surface properties of Mars from measured infrared signatures recorded by the Planetary Fourier Spectrometer (PFS) onboard the Mars Express mission in 2003. The RRT considers absorption, emission and multiple scattering of thermal and solar radiation by molecular (CO_2, H_2O, CO) and particulate (palagonite, montmorillonite) species. Precalculated sets of absorption cross-sections which are based on quasi-monochromatic line-by-line calculations are used to predict molecular transmission functions at 2.0 cm^{-1} spectral resolution in a layered atmosphere. Synthetic infrared spectra have been calculated in the 200–8000 cm^{-1} wavenumber range (1.25–50 μm) for a variety of atmospheric models and surface conditions. The influence of multiple aerosol scattering on the spectra is investigated on the basis of a successive approximation technique. Numerical results are compared with the spherical harmonics discrete ordinate method. Different retrieval procedures and results of a simultaneous retrieval of vertical temperature profiles and aerosol optical depths as well as surface temperature, pressure and reflectance are discussed. Real measurements performed by the IRIS instrument onboard Mariner 9 are also examined. © 2000 Elsevier Science Ltd. All rights reserved.

1. Introduction

Since that time when the first spacecrafts approached the red planet (1963 Mars 1, 1965 Mariner 4), several space missions using both orbiters and landers (Mariner 6,7,9; Mars 2,3,5,6; Viking 1,2; Phobos 2) have allowed to collect much information about the atmosphere and surface of Mars. A very detailed description of these and other failed missions and a collection of related scientific papers was given by Snyder and Moroz (1992). Many instruments were flown including infrared spectrometers like Infrared Interferometer Spectrometer (IRIS) onboard the Mariner 9 spacecraft in 1971/1972 (Hanel et al., 1972a, b) and Thermal Emission Spectrometer (TES) on Mars Global Surveyor (Christensen et al., 1998). The IRIS instrument made available one of the best existing data set up to now for studying the vertical structure of the Martian atmosphere on a global scale (Santee and Crisp, 1993). Despite these achievements and recent new findings from Mars Pathfinder and Mars Global Surveyor there are still some uncertainties in the data and many questions regarding atmospheric and surface properties of Mars remain unsolved.

The beginning of the new millenium marks the beginning of a new era of spacecraft exploration of the planet Mars. These missions will greatly extend the amount of observations of the Martian atmosphere and surface. The Planetary Fourier Spectrometer (PFS) is one of the instruments recently selected to fly on ESA's 2003 Mars Express mission. It will study spatial and temporal variations of the structure and the composition of the Martian atmosphere (Formisano et al., 1996; Hirsch et al., 1996). PFS will cover for the first time a wide spectral range to investigate reflected solar radiation in a short-wavelength channel (SWC, 1.25–5 μm, 2000–8000 cm^{-1}) and planetary thermal radiation in a long-wavelength channel (LWC, 5.0–45 μm, 220–2000 cm^{-1}) simultaneously at the spectral resolution of 2.0 cm^{-1}. Although this is not an instrument paper, some of the PFS main instrumental parameters in comparison with FTIR spectrometers on previous planetary missions and a short information about observing strategy are given in Appendix A.

* Corresponding author. Tel.: +49-30-6705-5369; fax: +49-30-6705-5385.

E-mail address: rainer.haus@dlr.de (R. Haus).

The main scientific goals of PFS are:

– global long-time monitoring of the three-dimensional temperature field in the atmosphere,
– monitoring of compositional variations of water vapour and carbon monoxide and search for other minor constituents in the atmosphere,
– study of optical properties of atmospheric aerosols and determination of their size distribution and chemical composition,
– study of surface properties (material composition, reflection features),
– investigation of the atmospheric radiative balance and dynamics considering aerosols.

The calculation of synthetic spectra in the infrared bands of molecules and aerosols and their iterative comparison with measurements is a fundamental background for the study of planetary atmospheres. To prepare the PFS data interpretation, a radiative transfer simulation and retrieval technique (RRT) was developed that is suitable to derive atmospheric and surface properties of Mars from measured infrared signatures. Parts of this technique, which is described in the present paper in some more detail, were applied by the authors some years ago to investigate the middle atmosphere of Venus based on the Venera-15 spectra (Haus and Goering, 1990; Titov et al., 1992; Zasova, 1994, 1995; Schäfer et al., 1995; Titov, 1995; Lellouch et al., 1997). Some of the RRT modules were also used in the field of environmental research to determine plume temperature and gas concentrations from remote sensing data on smoke stack and flare exhaust emissions obtained by a ground based, high-resolution, mobile Fourier spectrometer (Haus et al., 1994, 1998).

The RRT considers absorption, emission and multiple scattering of thermal and solar radiation by molecular (CO_2, H_2O, CO) and particulate (palagonite, montmorillonite) species. The present development status of the RRT does not cover cloud features. Water ice aerosols are very common in the Martian atmosphere (Zurek et al., 1992) and many IRIS spectra do exhibit broad 12 μm features due to ice clouds. One can even expect to find CO_2 ice signatures over polar regions. The effects of ice clouds on the simulated spectra and the comparison with measurements will be a subject of a subsequent paper.

The retrieval algorithms with respect to Martian conditions have been verified both on the basis of the so-called "synthetic measurements", which were created by the RRT, and by using real measurements performed by the IRIS instrument in 1971/1972. The paper discusses several examples of synthetic infrared spectra and presents methods and results of a simultaneous retrieval of temperature profiles, aerosol optical depths, surface parameters (related to both atmosphere and soil, i.e. temperature, pressure, reflectance) and minor constituent mixing ratios from radiation signatures in the region of the 15.0, 9.5, 2.7, 2.0 and 2.6 μm atmospheric bands.

2. Method of spectra simulation

2.1. Equation of radiative transfer

The propagation of radiation in a planetary atmosphere is influenced by absorption, emission and scattering by molecular and particulate species and is described by the radiative transfer equation. Confining to unpolarized radiation and assuming stationarity and elasticity of scattering in plane-parallel atmospheric layers where the conditions of local thermodynamic equilibrium (LTE) are maintained, the monochromatic radiation intensity (radiance) I at any altitude reference level z_r of the atmosphere is given by

$$I(z_r, \pm\mu, \varphi) = I^{BC}(z_{BC}, \pm\mu, \varphi)\tau(z_r, z_{BC}, \mu) + \int_{z_r}^{z_{BC}} J^S(z, \pm\mu, \varphi)W(z, \pm\mu)\,\mathrm{d}z', \quad (1)$$

where I^{BC} is the radiance due to the boundary condition and the integral represents the contribution of many atmospheric layers. ϑ and φ are the zenith and azimuth angles of propagation ($\mu = \cos\vartheta$) where $+\mu$ denotes upward radiation.

The quantity τ in Eq. (1) is the transmittance of an atmospheric layer extending from z_1 to z_2,

$$\tau(z_1, z_2, \mu) = \exp[-u(z_1, z_2)/\mu], \quad (2)$$

where $u = u^{\mathrm{ext}}$ is the optical depth of extinction in that layer,

$$u^{\mathrm{ext}}(z_1, z_2) = \int_{z_1}^{z_2} \beta^{\mathrm{ext}}(z)\,\mathrm{d}z,$$
$$\beta^{\mathrm{ext}} = \beta_g^{\mathrm{abs}} + \beta_g^{\mathrm{sca}} + \beta_p^{\mathrm{abs}} + \beta_p^{\mathrm{sca}}. \quad (3)$$

The volume extinction coefficient β^{ext} contains contributions from absorption (abs) and scattering (sca) of gaseous (g) and particulate (p) constituents. Molecular (Rayleigh) scattering can be neglected in the infrared due to its λ^{-4} dependence. The quantity W in Eq. (1) is the transmittance divergence,

$$W(z, +\mu) = \mathrm{d}\tau(z_t, z, \mu)/\mathrm{d}z, \quad W(z, -\mu) = \mathrm{d}\tau(z_b, z, \mu)/\mathrm{d}z. \quad (4)$$

$W(z, +\mu)$ describes the change of the total atmospheric transmittance between level z and the upper boundary level z_t (top of the atmosphere) around level z. $W(z, -\mu)$ is the analogous quantity for the lower boundary level z_b (bottom, surface). This so-called weighting function W is a measure of single-layer contribution to the radiance at a reference level z_r. Therefore, it plays an important role in the retrieval of vertical temperature and concentration profiles in planetary atmospheres.

The radiation source function J^S in Eq. (1) includes contributions from thermal emission (THE), single scattering (SS) and multiple scattering (MS) which have a more or less significant influence on radiative transfer

depending on wavenumber region, altitude and atmospheric composition,

$$J^{S} = J^{THE} + J^{SS} + J^{MS} = \gamma B + \omega J^{dir} + \omega J^{dif}. \quad (5)$$

Thermal emission under LTE conditions is characterized by the isotropic Planck function B,

$$B[T(z_r)] = C_1 v^3 / \{\exp[C_2 v / T] - 1\}, \quad (6)$$

where v is the wavenumber and T the temperature. The quantities $C_1 = 2hc^2$ and $C_2 = hc/k$ are the two radiation constants (h, k the Planck/Boltzmann constants, c the velocity of light). The second term in Eq. (5) describes the single scattering of direct solar radiation,

$$J^{dir}(z_r, \pm\mu, \varphi) = (4\pi)^{-1} \Phi(\pm\mu, \varphi, -\mu'_0, \varphi'_0) E^{\odot} \tau(z_r, z_t, \mu_0) \quad (7)$$

with $E^{\odot}$ the solar irradiance at the top, $\langle \mu'_0, \varphi'_0 \rangle = \Omega'_0$ the solid angle of solar incidence and Φ the scattering phase function. The third term in Eq. (5) includes the diffusely scattered light from all directions,

$$J^{diff}(z_r, \pm\mu, \varphi) = (4\pi)^{-1}$$
$$\times \int_0^{2\pi} \int_{-1}^{+1} \Phi(\pm\mu, \varphi, \pm\mu', \varphi') I(z_r, \pm\mu', \varphi') d\mu' d\varphi'. \quad (8)$$

The μ-integral runs over the upper ($+\mu$) and lower ($-\mu$) hemisphere. The scattering phase function Φ is a measure of radiation direction changes due to scattering. The direction of incidence is given by μ' and φ' while the new direction after scattering is described by μ and φ. The Henyey–Greenstein function is widely applied to describe aerosol scattering in planetary atmospheres (Irvine, 1975; Gerstl and Zardecki, 1985),

$$\Phi^{HG}(\cos\Theta) = (1 - g^2)(1 + g^2 - 2g\cos\Theta)^{-3/2}, \quad (9a)$$

$$\Theta = \arccos[\mu\mu' + \sqrt{1-\mu^2}\sqrt{1-\mu'^2}\cos(\varphi - \varphi')], \quad (9b)$$

where Θ and g are the scattering angle and the asymmetry parameter, respectively. g is the weighted mean cosine of the scattering angle. $g = 1$ characterizes pure forward scattering while $g = 0$ yields isotropic scattering.

The quantities ω and γ in Eq. (5) are defined as

$$\omega = \beta^{sca}/\beta^{ext}, \quad \gamma = \beta^{abs}/\beta^{ext} = 1 - \omega \quad (10)$$

with ω being the single scattering albedo of an atmospheric layer. It is connected to the aerosol single scattering albedo $\omega_0 = \beta_p^{sca}/(\beta_p^{abs} + \beta_p^{sca})$ by the relation

$$\omega = \omega_0/(1 + D), \quad D = \beta_g^{abs}/(\beta_p^{abs} + \beta_p^{sca}). \quad (11)$$

The upper boundary radiance I^{BC} in Eq. (1) is determined by direct solar radiation only, the diffuse radiance from space is zero. When the general case of an absorbing and scattering atmosphere is considered, the direct radiance is already accounted for via the source function J^{dir} defined by Eq. (7). Hence,

$$I^{BC}(z_t, -\mu', \varphi') = 0.0. \quad (12a)$$

The investigation of a pure gaseous atmosphere, on the other hand, would require an upper boundary term of the form

$$I^{BC}(z_t, -\mu', \varphi') = I^{\odot}(z_t, -\mu'_0, \varphi'_0) \, \delta(-\mu', -\mu'_0) \, \delta(\varphi', \varphi'_0). \quad (12b)$$

The delta functions ensure that this term disappears for all observation directions outside the direction of solar incidence.

The lower boundary radiance at the planetary surface or at a dense cloud layer top is determined by the incident downward flux from the upper hemisphere F^-, the reflectance features $Y(\mu, \varphi, \mu', \varphi')$ of the boundary and the thermal emission of the boundary. Hemispheric radiation fluxes are calculated according to

$$F = \int_{\Omega} I(\Omega) \cos\vartheta \, d\Omega = \int_0^{2\pi} \int_0^{\pi/2} I(\mu, \varphi) \cos\vartheta \sin\vartheta \, d\vartheta \, d\varphi$$
$$= \int_0^{2\pi} \int_0^1 I(\mu, \varphi) \mu \, d\mu \, d\varphi. \quad (13)$$

Thus, the downward flux at the lower boundary is given by

$$F^-(z_b) = E^{\odot} \mu'_0 \tau(z_b, z_t, \mu_0) + F^{sky}, \quad (14)$$

where F^{sky} is the diffuse flux of sky radiation. The presence of the first term in Eq. (14) ensures that direct solar radiation is included in the algorithm even in case of a pure gaseous atmosphere (where $\omega = 0$).

The anisotropic reflection function $Y(\mu, \varphi, \mu', \varphi')$ is approximated by an isotropic Lambert reflectance (albedo) A_b here by the assumption that reflection at a solid surface is more similar to isotropic reflection than it is to specular reflection. Nearly specular reflection takes place on water surfaces. Using this approximation, the upward flux of reflected radiation depends on the direction-independent reflectance A_b and the downward flux (direction-integrated downward radiance). The isotropic surface radiance related to this upward flux is $I^+ = F^+/\pi$. Thermal emission of the underlying surface is described by the Planck function at surface temperature $T(z_b)$ and the corresponding emissiviy $\varepsilon_b = 1 - A_b$. The complete lower boundary condition radiance is then given by

$$I^{BC}(z_b, +\mu, \varphi) = \frac{A_b}{\pi} E^{\odot} \mu'_0 \tau(z_t, z_b, \mu_0)$$
$$+ \frac{A_b}{\pi} \int_0^{2\pi} \int_0^1 I(z_b, -\mu', \varphi') \mu' \, d\mu' \, d\varphi'$$
$$+ [1 - A_b] B(T_b). \quad (15)$$

Due to the presence of term 2 in Eq. (15), the diffuse sky radiation must be calculated prior to evaluating upwelling radiances.

2.2. Multiple scattering

Several methods are used in the literature to include multiple scattering by atmospheric aerosols into radiance

simulation procedures, among them layer adding, successive approximation (SA), discrete ordinates (DISORD), and Monte Carlo (MC) techniques (Hansen and Travis, 1974; Irvine, 1975). The calculations presented here are mainly based on the SA method, but several results were also obtained using DISORD (Stamnes et al., 1988) and SHDOM (spherical harmonics discrete ordinate method, Evans, 1998). The basic principle of the SA technique is to examine the radiance contribution of photons that are scattered at each altitude level only once ($N = 1$) at first, then a second time ($N = 2$) and so on, i.e.

$$I(z, \Omega) = \sum_{i=0}^{N} I^{(i)}(z, \Omega). \tag{16}$$

The term $I^{(0)}$ is part of single scattered radiation. It considers contributions of atmospheric local thermal emission and single scattering of direct solar radiation as well as surface reflection of attenuated solar irradiance and sky radiation and thermal surface radiation,

$$I^{(0)}(z_r, \pm\mu, \varphi) = I^{BC(0)}(z_{b(t)}, \pm\mu, \varphi)\tau(z_r, z_{b(t)}, \mu)$$
$$+ \int_{z_r}^{z_{b(t)}} \{[1 - \omega(z)]B(z)$$
$$+ \omega(z)J^{dir}(z, \pm\mu, \varphi)\}W(z, \pm\mu)\,dz'. \tag{17}$$

The boundary terms $I^{BC(0)}$ are given by Eqs. (12a), (12b) and (15).

The contribution of multiple scattering to the source function $J^{(i)} = \omega J^{dif}$ is approximated by assuming isotropic scattered radiances I^+ and I^- over upward and downward hemisphere, respectively (Isaacs et al., 1987). The μ'-integral from -1 to $+1$ in Eq. (8) is then replaced by the sum of two μ'-integrals from 0 to 1 (the two-stream approximation),

$$J^{(i)}(z, \pm\mu, \varphi)$$
$$\simeq \frac{\omega(z)}{4\pi} I^{(i-1)+}(z) \int_0^1 \int_0^{2\pi} \Phi(\pm\mu, \varphi, +\mu', \varphi')\,d\varphi'\,d\mu'$$
$$+ \frac{\omega(z)}{4\pi} I^{(i-1)-}(z) \int_0^1 \int_0^{2\pi} \Phi(\pm\mu, \varphi, -\mu', \varphi')\,d\varphi'\,d\mu'. \tag{18}$$

Introducing the azimuth-averaged phase function $\Phi^*(\pm\mu, \pm\mu')$ (Liou, 1973),

$$\Phi^*(\pm\mu, \pm\mu') = \frac{1}{2\pi} \int_0^{2\pi} \Phi(\pm\mu, \varphi, \pm\mu', \varphi')\,d\varphi', \tag{19}$$

and defining a backscatter function $\Psi(\mu)$ (Meador and Weaver, 1980),

$$\Psi(\mu) = \frac{1}{2} \int_0^1 \Phi^*(+\mu, -\mu')\,d\mu'$$
$$= 1 - \frac{1}{2} \int_0^1 \Phi^*(+\mu, +\mu')\,d\mu', \tag{20}$$

the diffuse source function can be written in the following form:

$$J^{(i)}(z, \pm\mu) \simeq \omega(z)\pi^{-1}\{F^{(i-1)\pm}(z)[1 - \Psi(\mu)]$$
$$+ F^{(i-1)\mp}(z)\Psi(\mu)\}, \tag{21}$$

where the substitution $I^\pm = F^\pm/\pi$ was used again. $F^\pm$ are the hemispheric fluxes according to Eq. (13).

The radiance $I^{(1)}$ is determined in the next step from Eq. (1) where $J^S(z, \pm\mu, \varphi)$ is replaced by $J^{(1)}(z, \pm\mu)$ and the appropriate boundary conditions are used,

$$I^{(1)}(z_r, \pm\mu) = I^{BC(1)}(z_{b(t)}, \pm\mu)\tau(z_r, z_{b(t)}, \mu)$$
$$+ \int_{z_r}^{z_{b(t)}} J^{(1)}(z, \pm\mu)W(z, \pm\mu)\,dz', \tag{22a}$$

$$I^{BC(1)}(z_b, +\mu) = A_b/\pi F^{sky}(z_b) = A_b/\pi F^{(1)-}(z_b),$$
$$I^{BC(1)}(z_t, -\mu) = 0. \tag{22b}$$

$I^{(1)}$ is the complete radiance for degree $N = 1$ of multiple scattering, $I^{(2)}$ the complete one for $N = 2$, and so on. Note that the definition of complete single scattering includes the component $I^{(1)}$ (see for example, Sobolev, 1963).

The calculated upwelling top radiance at sufficient high order N of multiple scattering corresponds to the radiance which is measured by an orbiting instrument. It is given by

$$I^{(N)}(\infty, +\mu) = \frac{A}{\pi} F^{sky}(0)\tau(\infty, 0, \mu)$$
$$+ \int_0^\infty J^{(N)}(z, +\mu)W(z, +\mu)\,dz' \tag{23}$$

with $F^{sky} = F^{(N)-}$.

2.3. Transmittances

Following Eqs. (2) and (3) the monochromatic transmittance of an atmospheric layer extending from z_1 to z_2 is calculated from the expression

$$\tau(z_1, z_2, \mu) = \prod_{i=1}^{M} \exp\left[-\frac{1}{\mu} \int_{z_1}^{z_2} k_i(z)n_i(z)\,dz\right]. \tag{24}$$

$k_i(z)$ is the monochromatic, pressure and temperature-dependent absorption cross-section of component i (in units of cm^2), n_i the corresponding number density (in cm^{-3}) and M the number of infrared active components.

A fast and accurate method to determine molecular cross-sections $k(i, v, p, T)$ and transmittances in planetary atmospheres has been described in a recent paper by Titov and Haus (1997). A sophisticated line-by-line computer code is used which was thoroughly evaluated against the ITRA results (Spänkuch, 1987). The molecular line parameters are taken from the HITRAN 96 catalogue (Rothman et al., 1998). Quasi-monochromatic molecular absorption cross-sections have been calculated for the main molecular components of the Martian atmosphere (CO_2,

H_2O and CO). They are determined for several temperature and pressure values covering the expected range of Martian conditions. As a result, a three-dimensional database $K^{GAS}(v_{A-E}, p_{Min-Max}, T_{Min-Max})$ is created for each molecule that includes the regions 200–8000 cm^{-1}, 0.1–12 mb and 120–300 K. The wave-number step δv (i.e. the accuracy of monochromatic values) determines the accuracy of the final spectral-averaged transmittances and radiances. Several sets (e.g. with $\delta v = 0.0001, 0.01, 0.1$ cm^{-1}) were investigated. Titov and Haus (1997) have shown that a proper selection of atmospheric temperature/pressure models allows the reduction of the 3D base to a 2D one (excluding the pressure dimension). These databases are used to determine wavenumber-averaged transmittances and radiances for current atmospheric conditions, the topical line of sight and the spectral resolution $\Delta v = 2$ cm^{-1} of the PFS instrument.

Particulate components (aerosols) show a much weaker spectral dependence of absorption characteristics than molecular species. It is sufficient to determine mean aerosol cross-sections k^y for the point distance of spectral measurements (about 1 cm^{-1} for PFS). y stands as a synonym for extinction, absorption and scattering, respectively. The mean cross-section of extinction (in units of μm^2) normalized to one particle is described by the quantity $\langle \pi r^2 Q \rangle_i^{ext}$ (Hansen and Travis, 1974). It is calculated according to

$$k_i^{ext}(z) = \langle \pi r^2 Q \rangle_i^{ext}(z)$$
$$= \int_0^\infty \pi r^2 \langle Q \rangle_i^{ext}(x) n_i(z,r)\, dr \Big/ \int_0^\infty n_i(z,r)\, dr , \quad (25)$$

where $n_i(z,r)$ is the number density of particle mode i at level z at a particle radius extending from r to $r + dr$. The use of a multi-modal aerosol distribution is based on the fact that different types of aerosols with possible different size distributions can occur in a real planetary atmosphere. $\langle Q \rangle_i^{ext}(x)$ is the averaged extinction efficiency,

$$\langle Q \rangle_i^{ext}(x) = \int_0^\infty \pi r^2 Q_i^{ext}(x) n_i(z,r)\, dr \Big/ \int_0^\infty \pi r^2 n_i(z,r)\, dr , \quad (26)$$

which is calculated according to Mie theory (Hansen and Travis, 1974; Wiscombe, 1980) in dependence on the dimensionless parameter $x = 2\pi r/\lambda$ that describes the ratio of particle size and wavelength of incident radiation. n_i is determined by the aerosol size distribution function, $n_i = C_i f_i(r)$ where C_i is a constant associated with the total aerosol concentration N. A modified gamma function (Toon et al., 1977) is used in the simulations,

$$f_i(r) = r^\alpha \exp[-\alpha \gamma^{-1} (r\, r_{m_i}^{-1})^\gamma]. \quad (27)$$

α and γ are specific parameters of this distribution and r_{m_i} is the mean mode radius (e.g. 0.4 μm).

2.4. Wavenumber-averaged quantities

The transfer equations discussed above are strictly valid for monochromatic radiation. Real remote-sensing measurements, however, yield spectral-averaged data which correspond to the resolution of the instrument ($\Delta v = 2$ cm^{-1} for PFS) and its special spectral response function (instrumental lineshape function) ILS(v) that characterizes the measured radiance distribution within Δv. The spectral resolution Δv is usually defined as the half-width of the response function at the half-maximum of radiance (hwhm), i.e.

$$ILS(\Delta v/2) = 1/2\, ILS(0). \quad (28)$$

The real ILS can be approximated for modelling purposes by a Gauss function,

$$ILS(v) = \frac{1}{\sigma\sqrt{2\pi}} \exp\left[-\frac{v^2}{2\sigma^2}\right], \quad \sigma = \frac{\Delta v}{2\sqrt{2\ln 2}}. \quad (29)$$

The radiance R that is detected by the spectrometer at wavenumber v_0 is then given by

$$R(v_0) = \int_{\ll \Delta v \gg} ILS(v) I(v)\, dv \Big/ \int_{\ll \Delta v \gg} ILS(v)\, dv , \quad (30)$$

where $I(v)$ is the monochromatic radiance and $\ll \Delta v \gg$ the range where ILS contributions are nonzero (usually $2 - 3\,\Delta v$). Thus, R is calculated by convoluting the monochromatic radiance with the instrumental lineshape function.

3. Models of the Martian atmosphere

The calculation of synthetic spectra of the Martian atmosphere requires several model assumptions regarding the composition of gaseous and particulate components, temperature, pressure and concentration profiles as well as initial data on surface reflectance features.

Carbon dioxide is the dominant gaseous constituent in the Martian atmosphere with a mean volume mixing ratio of 95.3% (Owen, 1992). The determination of spatial and temporal variations of water vapour and carbon monoxide abundances and the search for other minor constituents is one of the main tasks of PFS measurements. At this time, the simulation software considers H_2O and CO with constant mixing ratios of 200 and 700 ppm, respectively. Characteristic temperature and pressure profiles of the Martian atmosphere were taken from MARSGRAM (Mars global reference atmosphere model, Johnson et al., 1989). Models for equatorial, middle and polar latitudes in the northern and southern hemisphere in summer and winter and during day and night were investigated. The selected Mars nominal model (NOM, surface temperature and pressure 214 K, 6 mb, Moroz et al., 1988) does only slightly distinguish from the MARSGRAM model for mid-latitude summer north.
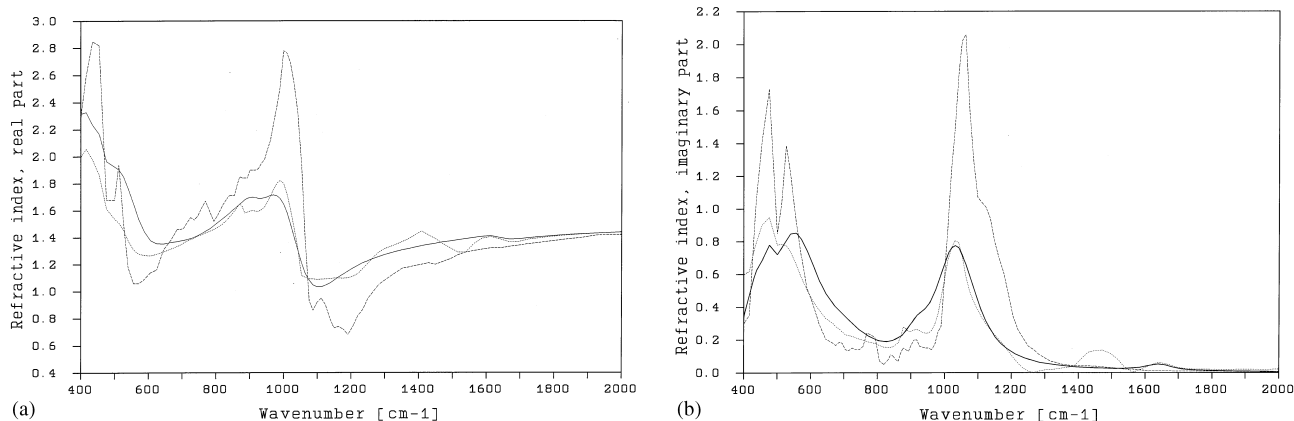
Fig. 1. (a) Real part of aerosol refractive index. Solid line: Palagonite (Roush et al., 1991), dotted line: palagonite (Arnold et al., 1995), dashed line: montmorillonite (Roush et al., 1991). (b) Imaginary part of aerosol refractive index. Notations see Fig. 1a.

Particulate components (aerosols) are always present in the Martian atmosphere at varying abundances in dependence on geographic location and elevation and over the seasons and from year to year (Kahn et al., 1992). Dust suspended in the atmosphere is responsible for multiple scattering of solar and thermal radiation. The identification of dust composition from remote-sensing data implies a characterization of the Martian soil properties. In order to include the effects of dust extinction in the calculation of atmospheric transmittances, the wavelength-dependent optical properties of the dust must be known. The real composition of dust which can be lifted to high altitude levels by heavy storms is not known today. Thus, different terrestrial analog materials are used in literature to explain the observed spectral signatures.

One of the early standard models was developed by Toon et al. (1977) who extracted information about the particle size distribution and composition of the airborne dust from the Mariner 9 IRIS data (Hanel et al., 1972a,b). A mixture of montmorillonite (a crystalline smectite clay) with 60% SiO_2 and basalt was found to achieve the best match to certain sets of averaged IRIS spectra. Palagonites (amorphous weathering products of basaltic glass) are also regarded as close spectral analog materials for the Martian dust at visible and infrared wavelengths (Evans and Adams, 1979; Singer, 1982). Observations with the infrared spectrometer (ISM) and other instruments onboard the Phobos 2 spacecraft have provided some more results of the characteristics of the Martian dust, suggestions on a modification of the size distribution used by Toon et al. and models of typical vertical profiles of the dust particles radius and number density (Drossart et al., 1991; Chassefière et al., 1995). Forget (1998) and Ockert-Bell et al. (1997) have published new models on synthetic optical properties of the Martian dust which do not assume a particular mineralogical composition of the particles.

Clouds (water and carbon dioxide ice aerosols) are known to occur in the polar hood regions. Water ice aerosols are also very common over tropical uplands during northern summer with opacities comparable to or greater than dust opacities (Zurek et al., 1992). H_2O ice features were clearly identified in the IRIS data around 12 μm and latest results from TES show cloud formation over the Tharsis region (Christensen et al., 1998). Cloud characteristics, however, are not incorporated in the present simulations, but work is underway.

Figs. 1a, b compare laboratory data (Roush et al., 1991; Arnold et al., 1995) on real (n) and imaginary (k) parts of the refractive index of montmorillonite and palagonite in the spectral region 5–25 μm (400–2000 cm^{-1}). Constant values are used across the wavenumber boundaries of laboratory data at present. Refractive indices of palagonite H2 were derived from ellipsometric reflectance measurements down to 2.5 μm (Arnold et al., 1995). The H2 real index exhibits a minimum at 3500 cm^{-1}, the imaginary index a maximum at 3400 cm^{-1}.

Extinction and scattering efficiencies $Q^{ext/scat}$ as well as aerosol single scattering albedo ω_0 and asymmetry parameter g were determined by applying Mie subroutines (Haus, 1995). Figs. 2 and 3 show the Mie results for Q^{ext} and ω_0 in the wavelength range 2.5–50 μm (200–4000 cm^{-1}). The influence of aerosol scattering in the region of the 15 μm CO_2 band (550–750 cm^{-1}) is small, but becomes larger with increasing wavenumber. A modified gamma size distribution function with a mode radius of 0.4 μm (size distribution maximum) and the parameters $\alpha = 2.0$, $\gamma = 0.5$ (Toon et al., 1977; Pollack et al., 1979) has been used as a standard configuration in the calculations, but test were also performed applying the modifications proposed by Drossart et al. (1991). The gamma function is popular for modeling terrestrial cloud particle size distributions. Several models of total optical depths u^A at 9.5 μm (the reference wavelength chosen here, $v_{ref} = 1050$ cm^{-1}) were examined covering variations in the range from 0.0 to 2.0. Aerosol column depths around 0.3 represent typical quiet conditions out of dust storm
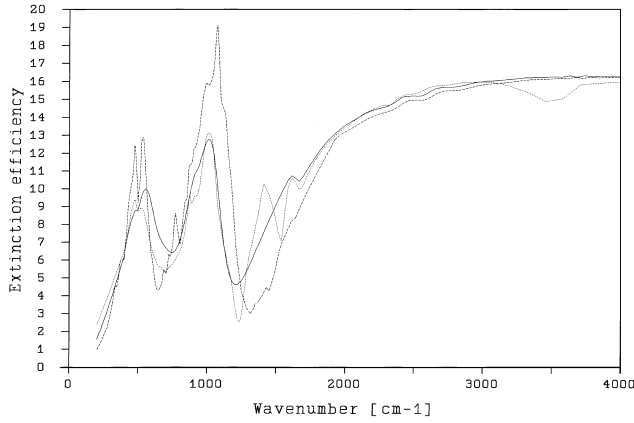
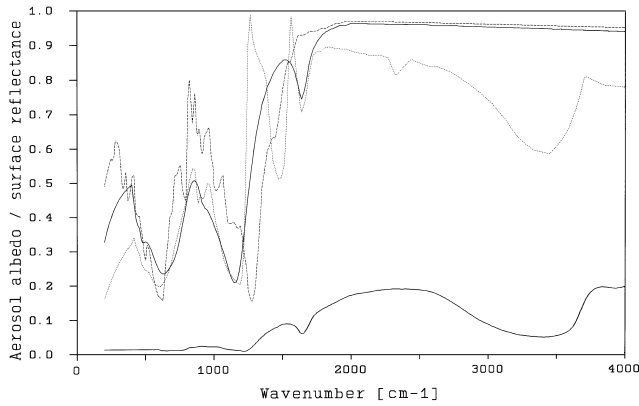Fig. 2. Aerosol extinction efficiency Q^{ext}. Notations see Fig. 1a.

Fig. 4. Contribution of solar and thermal radiation to the top radiance (neglect of atmospheric bands). Dashed lines: bright polar model ($A_s = 0.4, T_{Mars} = 140$ K), solid lines: dark equatorial model ($A_s = 0.1, T_{Mars} = 270K$).

Fig. 3. Aerosol single scattering albedo ω_0. Notations see Fig. 1a. Solid line at the bottom: Surface reflectance A_s of palagonit H2 (Arnold et al., 1995).

periods (Martin and Kieffer, 1979; Martin, 1986; Santee and Crisp, 1993). An exponential decrease of aerosol concentration with the scale height $H_{aer} = 13$ km is assumed.

The simulations use three models of the surface reflectance A_s,

- spectral constant ($\lambda < 5$ μm) for dark regions ($A_s = 0.1$),
- spectral constant ($\lambda < 5$ μm) for bright regions ($A_s = 0.4$),
- spectral variable, palagonite H2, DLR laboratory measurements (Arnold et al., 1995).

The palagonite reflectance curve which is also shown in Fig. 3 indicates that the surface emissivity ε_s at wavenumbers below 1300 cm^{-1} is greater than 0.98. This result is consistent with the Viking IRTM experiment indicating an ε_s value near unity (Kieffer, 1976). No attempt was made to include any spectral dependence of ε_s for this study and a value of 1.0 was adopted. Future improvements of the RRT will also include effects of varying surface emissivity in the thermal infrared (especially for dark surfaces) as it was done for example by Blecka et al. (1997).
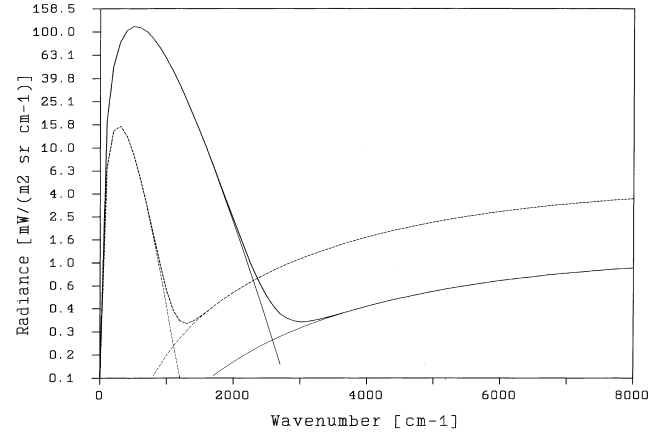
Solar irradiance data at the top of the Earth's atmosphere are taken from Thekaekara (1973) and corrected for the mean Sun–Mars distance. The calculations use a standard observation direction $\vartheta_{obs} = 0°$ (nadir), the standard solar zenith angle is $\vartheta_{sun} = 20°$.

4. Synthetic spectra of Mars

When atmospheric contributions are neglected, a constant surface albedo A_s is assumed, the surface emissivity is set equal to 1, and the solar irradiance is approximated by the Planck radiation at T_{SUN}, the upwelling radiance for nadir geometry can be written according to Eq. (15) in the form

$$I(v) = A_s r^2 R^{-2} B(T_{SUN}, v) + B(T_{MARS}, v). \qquad (31)$$

r is the radius of the Sun, R the mean distance Mars–Sun, $T_{SUN} = 5800$ K the effective black-body temperature of the Sun, and T_{MARS} the Martian surface temperature. The maximum of the solar radiation curve is located at much higher wavenumbers than that of thermal planetary radiation. As a consequence, there is a defined wavenumber v_{min} where the effective top radiance exhibits a minimum as it is demonstrated in Fig. 4. In the bright polar atmospheric model (dashed lines: $A_s = 0.4$, $T_{MARS} = 140$ K), this minimum is located near 1250 cm^{-1} (8 μm). The dark equatorial model (solid lines: $A_s = 0.1$, $T_{MARS} = 270$ K) shows this minimum at 3000 cm^{-1} (3.4 μm). An intermediate value for a standard atmosphere ($A_s = 0.25$, $T_{MARS} = 215$ K) is located at 2000 cm^{-1} (5 μm). Thus, the total spectrum can be divided into the long-wavelength range (thermal spectral region) and the short-wavelength range (solar spectral region). Due to the strong dependence of this radiance minimum on temperature and albedo, both terms should be taken into consideration in the wavenumber interval between 1300 and 2500 cm^{-1}. It is clear,
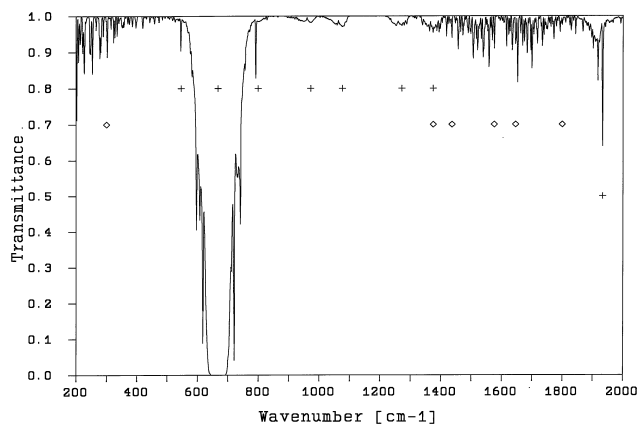
Fig. 5. Transmittance spectrum (free of dust) for model MA3. The symbols mark features of CO_2 (−+−) and H_2O (−◇−).
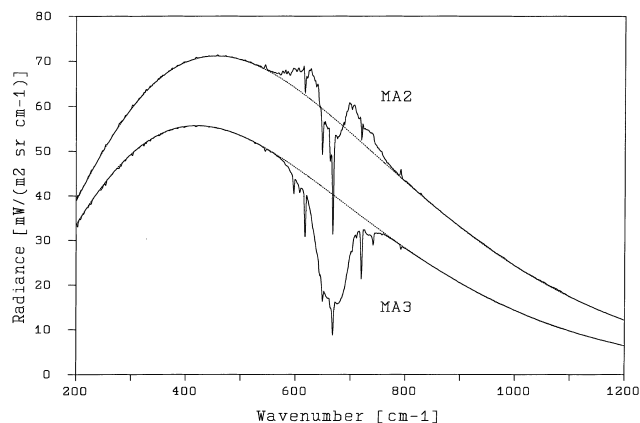

Fig. 6. Radiance spectra (free of dust) for models MA2 and MA3. The dashed lines are the Planck functions at the corresponding surface temperature.

however, that calculations in the 15 μm CO_2 band will neglect solar radiation, while calculations in the 2.7 or 2.0 μm CO_2 bands can be performed without access to thermal radiation.

4.1. Synthetic spectra in the thermal region (5–50 μm)

Figs. 5, 6 and 7a show top transmittance, radiance and equivalent brightness temperature simulation results for different models of a pure gaseous atmosphere (MA1-4, Fig. 7b) in the thermal spectral region. The dotted curves in Fig. 6 are the Planck functions at corresponding surface temperature. The most striking feature in these spectra is the 15 μm carbon dioxide band centred at 668 cm^{-1}. This band will be used to retrieve atmospheric temperature profiles. Both the regions from 200 to 500 cm^{-1} (rotational band) and from 1400 to 1800 cm^{-1} (6.3 μm band) are exclusively determined by water vapour, but its influence on the radiance spectrum is extremely small. The

weak signatures between 900 and 1400 cm^{-1} and the band near 1900 cm^{-1} are due to CO_2. The radiance outside the strong 15 μm band completely originates from surface radiation. Thus, surface temperatures of 259 K (MA1), 232 K (MA2), 214 K (MA3, nominal model NOM) and 177 K (MA4) are deduced from Fig. 7a. The radiances in the 15 μm region result from higher atmospheric levels (30–50 km in the main centre at 668 cm^{-1}). The inversion in the MA4 profile indicates that the bulk of the atmosphere is warmer than the underlying surface and remarkable emission instead of absorption signatures occur in the 15 μm wings due to the low surface temperature. The increase of brightness temperature in the MA2 curve in the spectral regions around 630 and 700 cm^{-1} is also created by a temperature inversion, i.e. the temperature in the lower layers is higher than the ground temperature. It is clear from these comments that the 15 μm CO_2 band plays an important role for the remote sensing of temperature profiles in planetary atmospheres. Details are discussed in Section 5.1.

The influence of atmospheric aerosols is simulated using parameters of palagonite (Roush et al.,1991). Brightness temperature spectra for the nominal model NOM and six aerosol models 0, A, B, C, D and E for total (column) optical depths of 0.0, 0.1, 0.3, 0.5, 1.0 and 2.0 at the reference wavenumber 1050 cm^{-1} are shown in Fig. 8. The calculations are based on a conservative scattering approach (see text below). Aerosol suspended in the atmosphere causes a significant modification of pure gaseous spectra when the total optical depth exceeeds 0.1 with a maximum influence at around 500 and 1030 cm^{-1} which is due to the efficiency maxima at these wavenumbers (see Fig. 2). These regions are well suited to determine aerosol features from measured spectra, because they are little influenced by gas signatures.

Fig. 9 shows a comparison of brightness temperatures (model NOM, aerosol models B and D, u^A = 0.3, 1.0) in dependence on the aerosol scattering mode used in the calculations. The solid curves yield the multiple scattering results (degree $N = 5$) which are not modified by considering higher orders of successive scattering. The dotted curves are obtained when the "complete absorption" mode (conservative scattering) is used. This mode treats scattered radiation as if it were absorbed at the place of scattering. The maximum brightness temperature difference between these modes for model D is less than 1.5 K (B : 0.5 K) in the region below 1300 cm^{-1}. Even for high aerosol densities (model E) it is possible to approximate multiple scattering calculations by a conservative scattering model in the main part of the thermal spectral region. This approximation becomes more and more reliable with decreasing aerosol depths. It has a large practical importance: major savings in computer time can be achieved during the calculation of synthetic spectra and the retrieval of atmospheric parameters from measured spectra. It should be mentioned, however, that a much larger influence of
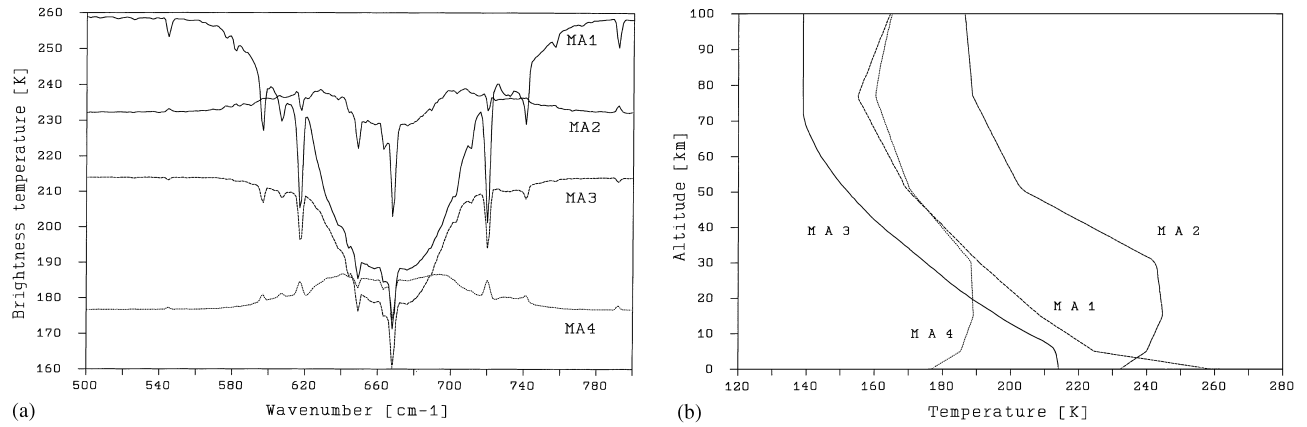
Fig. 7. (a) Brightness temperature spectra (free of dust) for models MA1-MA4. (b) Temperature profiles of atmospheric models MA1-MA4.
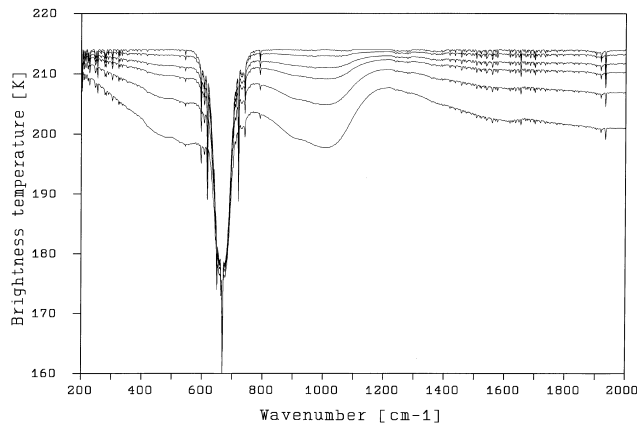

Fig. 8. Brightness temperature spectra as a function of aerosol (palagonite) optical depth at 1050 cm^{-1}. Top to bottom: $u^A = 0.0, 0.1, 0.3, 0.5, 1.0, 2.0$.
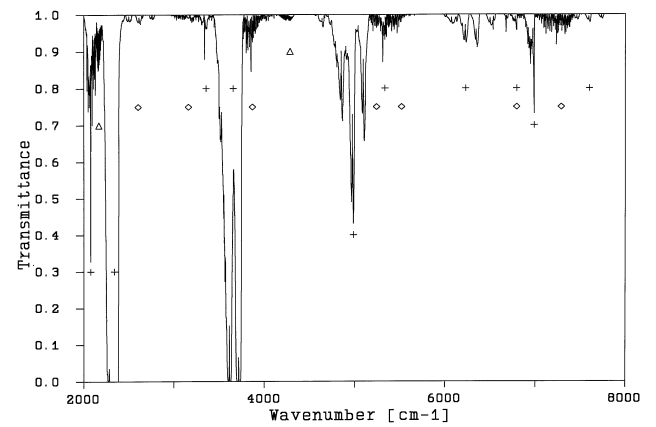

Fig. 10. Transmittance spectrum (free of dust) for model MA3. The symbols mark features of CO_2 ($-+-$), H_2O ($-\diamond-$), and CO ($-\triangle-$).
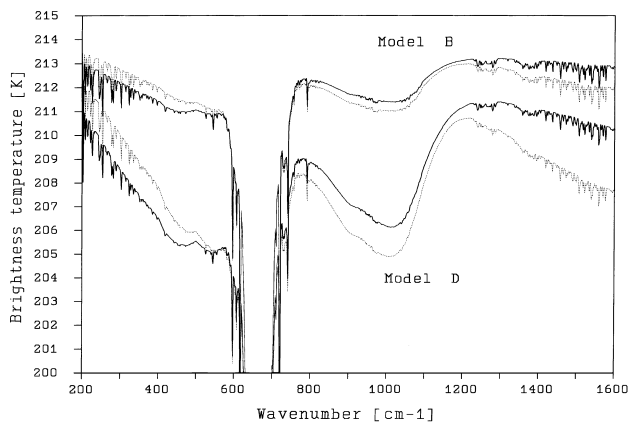

Fig. 9. Brightness temperature spectra as a function of aerosol (palagonite) scattering mode. Solid lines: multiple scattering, dashed lines: conservative scattering.

scattering effects may occur for other aerosol composition models (ice, for instance) and this approximation does not longer hold true.

4.2. Synthetic spectra in the solar region (1.25–5μm)

Fig. 10 shows the transmittance spectrum for the pure gaseous atmosphere (model NOM) in the solar region. This simulation includes the molecules CO_2, H_2O and CO. Strong CO_2 bands occur at 4.8 μm (2100 cm^{-1}), 4.3 μm (2325 cm^{-1}), 2.7 μm (3700 cm^{-1}) and 2.0 μm (5000 cm^{-1}). Smaller signatures are observed at 1.9, 1.6 and 1.3 μm (around 5300, 6200, 7600 cm^{-1}). Significant water vapour bands are located at 2.6 and 1.9 μm. Other H_2O bands occur at 4.8, 3.8, 3.1 and 1.4 μm. Narrow CO bands can be observed at 4.7 and 2.4 μm (2170 and 4170 cm^{-1}). While the H_2O and CO signatures can be used to retrieve column densities and possibly information on vertical concentration profiles, the 2.0 and 2.7 μm CO_2 bands are suitable to determine the surface pressure and aerosol optical depths. Details are given in Sections 5.3 and 5.4.

Fig. 11 shows clear atmosphere top radiances (model NOM) for three surface reflectance models. The broken and solid lines result from the spectral constant bright and dark models with $A_s = 0.4$ and 0.1, respectively. Palagonite is
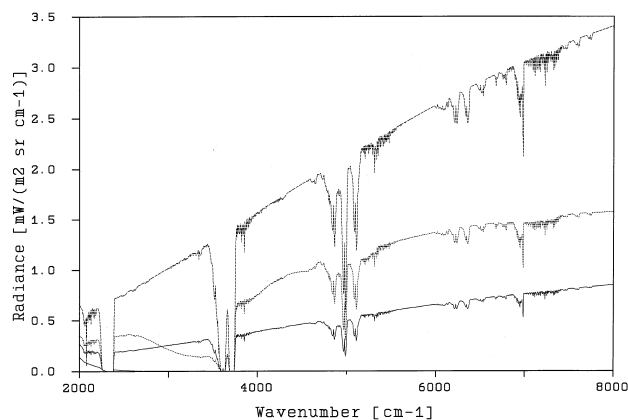
Fig. 11. Radiance spectra (free of dust) for model MA3 as a function of surface reflectance model. Solid line: $A_s = 0.1$, dashed line: $A_s = 0.4$, dotted line: $A_s = f(v)$, palagonite H2, solid line in the left lower corner: thermal radiation.
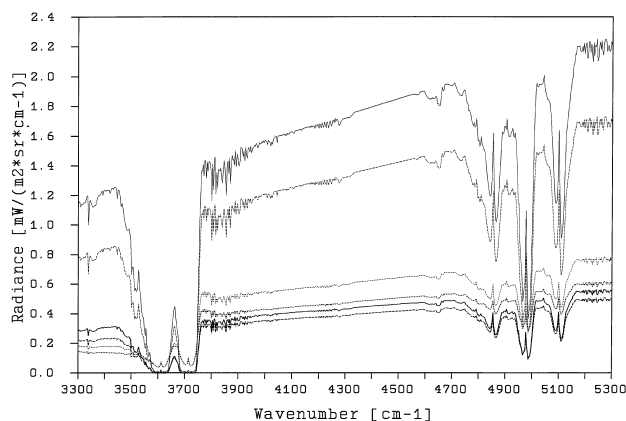

Fig. 12. Radiance spectra as a function of aerosol (palagonite) optical depth u^A at 1050 cm^{-1} for two surface reflectance values A_s (upper 3 thin lines: 0.4, lower 3 thick lines: 0.1), solid lines: pure gas, dashed lines: $u^A = 0.3$, dotted lines: $u^A = 2.0$.

an analog material for regions on the Martian surface that are covered by weathering products. The dotted line is obtained, when the spectral dependence of the palagonite H2 reflectance is considered (see Fig. 3). The influence of the 2.9 μm silicate band is clearly visible in this case. The curve in the left lower corner describes the contribution of thermal radiation. It follows that thermal radiation can be neglected below 4 μm in this case. On the other hand, it is clear from Fig. 4 that the spectral range around 4 μm contains significant parts of thermal radiation over dark equatorial regions. This fact can be useful to retrieve atmospheric temperature profiles from night time measurements using the 4.3 μm CO_2 band.

The change in the spectral behaviour due to atmospheric aerosol influence is shown in Fig. 12 for palagonite H2 aerosol models B and E ($u^A = 0.3$ and 2.0 at 9.5 μm). The multiple scattering calculations were performed using a number of successive orders of $N = 10$ and constant sur-

face reflectance values of 0.1 (thick lines) and 0.4 (thin lines). Palagonite causes a strong modification of the spectra in comparison with a clear atmosphere. While bright surface features as well as gas signatures (except of the 2.7 μm CO_2 band centre) are generally darkened by atmospheric aerosol layers, multiple scattering at large optical aerosol depths may lead to a significant enhancement of dark surface radiances. The specific response of the radiation field is not only influenced by the surface reflectance A_s and the aerosol depth u^A, but it is also a function of aerosol microphysical properties like single scattering albedo ω_0 and phase function $\Phi(g)$. The single scattering albedo minimum at 2.9 μm (see Fig. 3) tends to reduce the radiances at large optical depths. Atmospheric aerosols can have an influence which is comparable with surface reflectance features of the same material (see Fig. 11), therefore. Consequently, serious difficulties may arise in separating dust and soil signatures. The saturated 2.7 μm CO_2 band (wavenumber region 3500–3800 cm^{-1}), on the other hand, offers a possibility to overcome this complicated problem (see Section 5.4).

The calculations indicate that accurate radiance results are obtained after several iterations in the multiple scattering procedure the number of which depends on aerosol model, surface reflectance features and spectral region. Sufficient accuracy is achieved for $N = 5$–10 in most cases. The use of a conservative scattering model, which is a good approximation in the thermal region, is not possible in the solar region. Thus, the calculation of synthetic spectra and the retrieval of atmospheric parameters from measured spectra is more complicated and requires more computer time.

5. Retrieval methods and results

When temperature profiles and absorber concentrations along the atmospheric path are known, wavenumber-dependent radiances can be calculated from Eq. (1). This is the forward problem in radiative transfer simulation procedures. To estimate atmospheric parameters from measurements of thermal or reflected radiation, the inverse problem must be solved which is much more complicated. There are several techniques to approximate the inversion problem including relaxation and statistical methods as well as least-squares fit techniques. Some a priori information about the atmosphere has to be imposed in any case. The most widely applied relaxation techniques are the methods of Chahine (1968, 1970, 1972) and Smith (1970). These iterative procedures allow simultaneous retrievals of vertical profiles of both atmospheric temperature and absorber optical depths. The present calculations were performed using both the methods of Smith (1970) and Tikhonov and Arsenin (1977). The Tikhonov method provides a search for the solution of ill-posed problems among a set of functions with pre-defined smoothness.

5.1. Thermal sounding of the atmosphere at 15 μm

Under local thermodynamic equilibrium (LTE) conditions, the thermal radiation emitted by the surface or atmosphere of a planetary body is related to its kinetic temperature. The altitude from which the radiation escapes to space depends on the strength of an absorption band. The stronger the band the higher the level emitting directly to space. In a strong band, the radiation from the surface and lower atmospheric layers is absorbed by higher regions and cannot escape to space. However, the strength of an absorption band of atmospheric trace gases usually varies by several orders of magnitude within a certain spectral interval. When the outgoing radiation is measured in a spectral range covering the entire band, different parts of the band will bear information about the atmospheric temperature and composition at different altitudes (or pressure levels).

In general, any gas present in the atmosphere can be used for the thermal sounding but several conditions must be satisfied. First, the gas must have spectral bands in the thermal infrared region (6–50 μm). Second, it must be abundant enough to give strong absorption in the band centre to achieve a maximum altitude range of sounding. And third, it is desirable that the gas is uniformly mixed within the bulk of the atmosphere and its abundance must not vary significantly with space, local time and season. In the case of terrestrial planets, carbon dioxide meets these requirements rather well. That is why the 15 μm CO_2 fundamental band (centred at 668 cm^{-1}) is usually used for the thermal sounding of the atmospheres of Venus, Earth and Mars.

When multiple scattering by atmospheric aerosols can be neglected or is approximated by the conservative scattering model, the outgoing thermal radiation is described by the equation

$$R_t(v_i, \mu) = B(v_i, T_s)\tau(v_i, \infty, 0, \mu)$$
$$+ \int_0^\infty B[v_i, T(z)]W(v_i, z)\,\mathrm{d}z'. \tag{32}$$

Here, R, B, τ and W are wavenumber-averaged quantities according to the spectral resolution of the instrument at a certain channel v_i. The weighting function W is the measure for single layer contributions to the top radiance. Fig. 13 shows the weighting functions of selected wavenumbers (sounding channels) of the right-hand part (in the wavenumber picture) of the 15 μm CO_2 band for an equatorial day temperature model (MA1) and the PFS spectral resolution of 2 cm^{-1}. These weighting functions primarily depend on pressure, but for a selected atmospheric model (case MA1) the plot over altitude was chosen to show the contribution of different atmospheric layers to the total radiance measured (or simulated) at the top of the atmosphere. The MA1 band centre bears maximum information about the altitude range around 50 km. The relative width of W determines the vertical resolution of
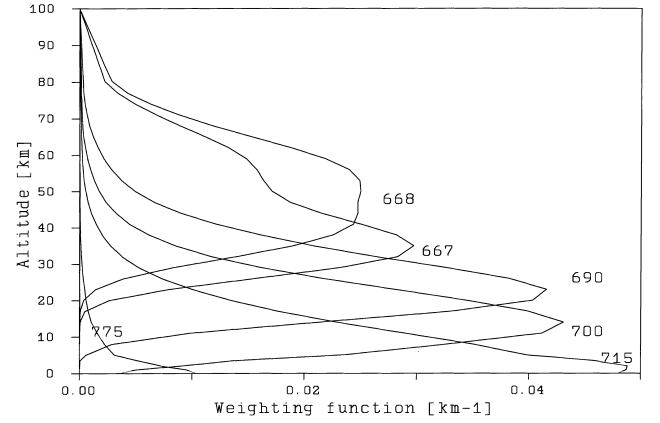

Fig. 13. CO_2 15 μm weighting functions for selected spectral channels v_i (wavenumbers in cm^{-1}).

extracted temperature profiles. The width becomes larger with increasing altitude.

According to Smith's method an initial temperature profile $T^j(z)$ ($j = 1$) is assumed to calculate top radiances R_t in the first step from Eq. (32). The second step starts with a comparison of measured and simulated radiances,

$$B^{j+1}(v_i, z) = B^j(v_i, z) + [R_t^{\mathrm{meas}}(v_i) - R_t^j(v_i)]. \tag{33}$$

This equation is based on the assumption that the deviation in the Planck function from one iteration to the following is constant throughout the atmospheric column at each wavenumber v_i. The altitude-dependent brightness temperatures $T^{j+1}(v, z)$ are then calculated by inverting Eq. (6) according to

$$T^{j+1}(v_i, z) = C_2 v_i / \ln [C_1 v_i^3 / B^{j+1}(v_i, z) + 1]. \tag{34}$$

The true temperature profile is determined from a weighted average of channel brightness temperatures where the weights are the weighting functions $W(v_i, z)$ and M is the number of spectral channels,

$$T^{j+1}(z) = \sum_{i=1}^M T^{j+1}(v_i, z) W(v_i, z) \bigg/ \sum_{i=1}^M W(v_i, z). \tag{35}$$

This procedure is repeated until convergence is achieved. A re-calculation of the weighting functions during each step is not necessary. It was found, however, that higher accuracies are obtained when a re-calculation is performed after the last iteration followed by a full repetition of the iteration procedure.

The Tikhonov regularization method starts from the linearization of the Planck function in the vicinity of the temperature profile,

$$B(T) = B(T_0) + \delta B/\delta T * \Delta T(z), \tag{36}$$

where $\Delta T = T - T_0$. Substitution of this expression into Eq. (32) yields the equation of thermal sounding,

$$\int_\infty^0 A(v_i, z) f(z)\,\mathrm{d}z = g(v_i),$$
$$A(v_i, z) = W(v_i, z)\delta B/\delta T[T_0(z)], \tag{37}$$

where A is the kernel of the integral equation. $f(z) = \Delta T(z)$ is the unknown vector of temperature correction and $g(v_i) = I^{meas}(v_i) - I^{sim}(v_i, T_0)$ the difference between the measured and simulated spectrum for the initial temperature profile $T_0(z)$.

The vector $f(z)$ which corrects the initial temperature profile is found from Eq. (37) which is a Fredholm equation of the first kind. Many remote-sensing tasks are reduced to this mathematical expression. The problem of solving the equation is known to be an ill-posed one. This means that small uncertainties in the right-hand side, which are always present since $g(v_i)$ contains the vector of measurements, can result in great errors in the solution. The method of Tikhonov regularization provides an algorithm that avoids the non-physical solutions and arranges the search of the unknown vector $f(z)$ on the class of functions with a certain degree of smoothness. A so-called Tikhonov function is introduced,

$$M^\alpha[f] = \rho^2[f, g] + \alpha\Omega[f] \tag{38}$$

with

$$\rho^2[f, g] = \int_v \left\{ \int_z A(v, z) f(z)\, \mathrm{d}z - g(v) \right\}^2 \mathrm{d}v,$$

$$\Omega[f] = \int_v \left\{ f^2 + \left(\frac{\delta f}{\delta z}\right)^2 \right\} \mathrm{d}v. \tag{39}$$

ρ^2 is called a deviation function and is the measure of the difference between the right-hand side of Eq. (37) and the value of the left-hand side for some solution $f(z)$. Ω is called the stabilizing function because it prevents the occurence of instabilities. The free parameter α is the regularization parameter. Its value depends on the noise of the measurements and is used to adjust the method to the particular experimental data. The final solution of Eq. (37) is the function $f(z)$ which minimizes the Tikhonov function (38). Minimization of this function means both minimizing the deviation function and imposing restrictions on the value of the first derivative of the solution.

Due to the lack of real PFS measurement data at this time, a number of so-called "synthetic measurements" was created by the simulation software. These synthetic top radiances were obtained for defined temperature profiles which are called the "basis". The iterative procedure starts with an "initial" or first-guess temperature profile. The final result is the "retrieved" profile. This notation will be used below when examples for the temperature retrieval are discussed.

The best retrieval results are obtained when the initial profile is close to real conditions. To adjust the initial profile the following procedure is used. A linear temperature decrease with altitude is assumed starting with a surface temperature T_s which is deduced from the measured top brightness temperature in spectral regions outside the atmospheric absorption bands. If palagonite was an adequate material to fit observed spectral signatures,

the region around 1220 cm^{-1} is optimal (see Fig. 8), hence, $T_0 = T_B$ (1220 cm^{-1}). The radiation of the spectral channels in the 15 μm CO_2 band, on the other hand, is determined by different atmospheric layers. As it was shown above the centre radiation in the Martian atmosphere reflects the thermal properties of the region between 25 and 50 km. The measured brightness temperature T_B at 668 cm^{-1} is used to find the approximate temperature value at 40 km, $T_{40} = T_B$ (668 cm^{-1}). Thus, the linear initial profile is determined by the two values T_0 and T_{40}. Above 50 km, this profile is adjusted to approach an isothermal behaviour at altitudes above 80 km. When the bulk of the atmosphere is warmer than the surface (e.g. profile MA4 in Fig. 7b), the initial profile up to 40 km is either built-up by the T_B (668 cm^{-1}) value (i.e. isothermal) or a triangular profile is used with T_{max} located near 30 km (see comments with respect to Fig. 14a).

The only use of the right-hand wing of the 15 μm CO_2 band (668–800 cm^{-1}) is sometimes more preferable for the temperature retrieval because the aerosol influence is weaker than in the left-hand wing (see Fig. 8). This holds true as long as palagonite or montmorillonite are considered in the simulations. When aerosol opacity of real Martian dust has comparable amounts in the two wings, there is no argument to prefer one or another side (except of requirements to save software running time) and the whole 15 μm band should be used. Strong H_2O ice features occur in some of the IRIS spectra at 825 cm^{-1}(12 μm). This is another argument for taking into account both the wings.

Fig. 14a and b show the comparison of basis and retrieved temperature profiles for four atmospheric models where the surface pressures are known. The retrieval results are in good agreement with the basis profiles up to 50 km. The methods of Smith and Tikhonov produce similar results up to this level except for the PWS profile. But in this case, the Smith retrieval was performed using an initial temperature model which was very close to the basis one (triangular profile), while the Tikhonov retrieval is based on an isothermal initial profile. At higher altitudes, the retrieval accuracy of both methods is not very high due to the lack of appropriate weighting functions.

The temperature retrieval at lower altitude levels is sensitive both to the surface pressure p_s and the aerosol optical depth u^A. p_s can be determined simultaneously from PFS measurements in the 2.0 μm region. The first step in the proposed group of main iterations to retrieve atmospheric and surface parameters of Mars from signatures in different spectral regions (see Table 1) is a temperature retrieval run. This means that in case of using real measurement data (and not specified atmospheric models as in case of Fig. 14) the value of surface pressure p_s is not known at first. Since the temperature profile will be recalculated following a pressure retrieval at 2.0 μm (a region which is not very sensitive against temperature), one can expect to find the real temperature profile (and the real
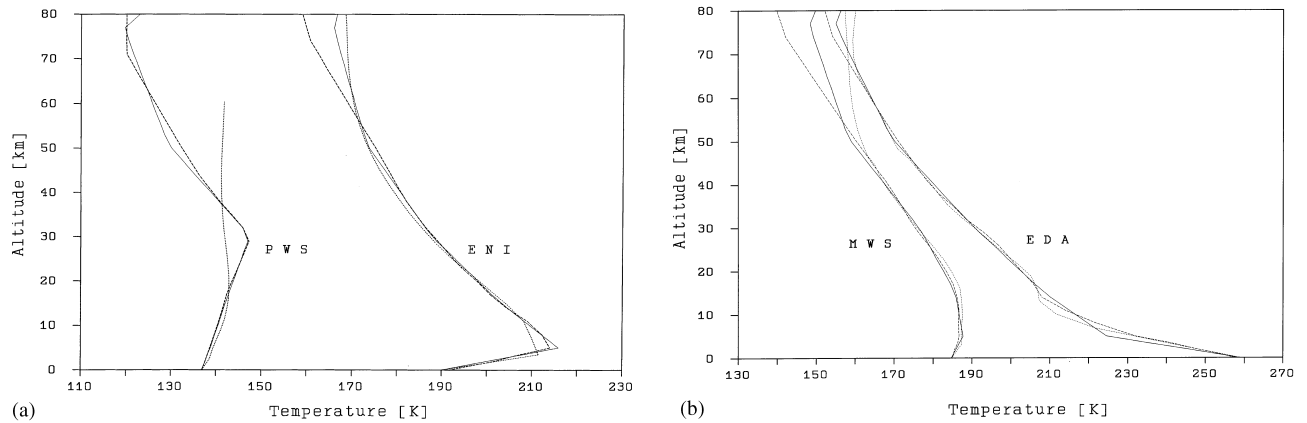
Fig. 14. (a) Comparison of basis and retrieved temperature profiles for two atmospheric models (polar winter south, equatorial night). Solid lines: basis, dashed lines: Smith method, dotted lines: Tikhonov method. (b) Same as Fig. 14a, but for atmospheric models midlatitude winter south, equatorial day.
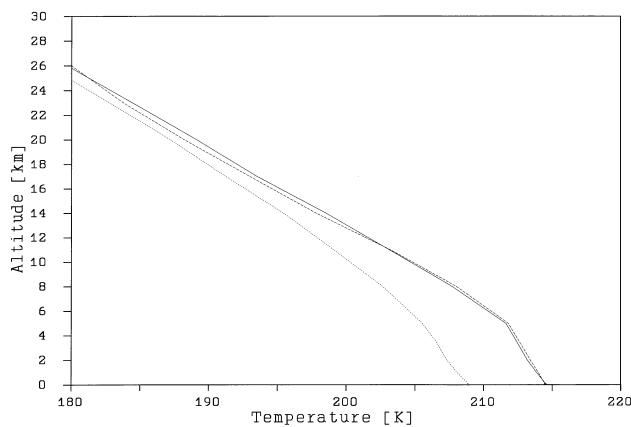

Fig. 15. Aerosol influence on temperature retrieval. Dashed line: basis profile MA3 with $u^A = 1.0$, solid line: aerosols considered, dotted line: aerosols not considered.

Fig. 16. Measured IRIS spectra of Mars. EN: equatorial north, SPC: south pole cap, NPC: north pole cap.

surface pressure) after several alternating iterations in the 15 and 2 μm regions. The present calculation scheme for conditions where p_s is not known (e.g. retrievals based on IRIS data, see Figs. 16–18) uses a standard pressure value of 6.1 mb and a barometric correction according to a terrain model of Mars. A change in surface pressure will shift the retrieved temperature profile along the altitude axis. Deviations up to 5 K were found when the p_s value was varied by 2 mb (or 30%).

Fig. 15 illustrates the different retrieval results when aerosols are considered (solid line) or neglected (dotted line). The basis radiance spectrum was generated for the temperature model NOM (MA3, dashed line) and the aerosol model D ($u^A = 1.0$ at 9.5 μm). When aerosols are neglected in the retrieval procedure, the deviation of the retrieved profile is stronger near the surface, but becomes smaller above 15 km due to the assumed exponential decrease of aerosol density with altitude. The opacity of 1.0 used here is that of an intense dust storm. The maximum difference in the retrieved profiles, however, does not exceed
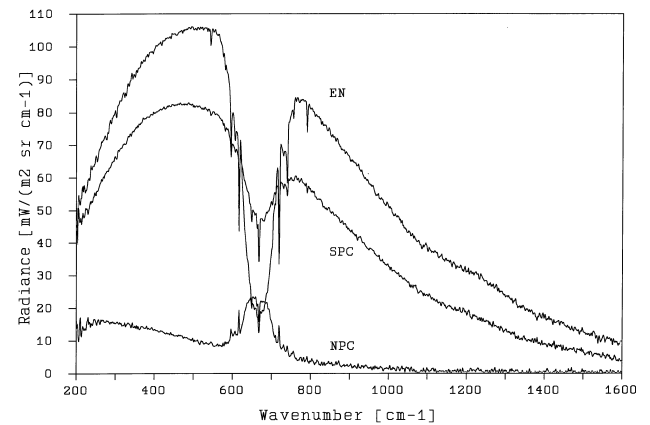
7 K in the layers near the surface. The deviations for other atmospheric models investigated are in the same order of magnitude (not more than 10 K). The differences do not exceed 3 K at $u^A = 0.3$.

It is concluded that uncertainties due to pressure and aerosol optical depth produce comparable errors in the retrieved temperature profiles at lower altitudes. Since the expected PFS noise equivalent spectral radiance (NESR) is around 0.2–0.4 mW/(m² sr cm⁻¹) at 15 μm, signal fluctuations will not affect the retrieval results.

One of the most comprehensive data sets on Martian infrared spectra up to now was recorded in 1971/1972 by the IRIS instrument onboard the Mariner 9 orbiter (Hanel et al., 1972a, b). These measurements contain about 20.000 highly resolved radiance spectra ($\Delta v = 2.4$ cm⁻¹) that cover almost the complete range of thermal radiation of Mars (200–1960 cm⁻¹, 5.1–50 μm). Fig. 16 presents three measured IRIS spectra which were recorded over the northern equatorial region (EN: +2.0°N) and over the southern and northern polar caps (SPC: −74.8°S, NPC: +66.1°N),
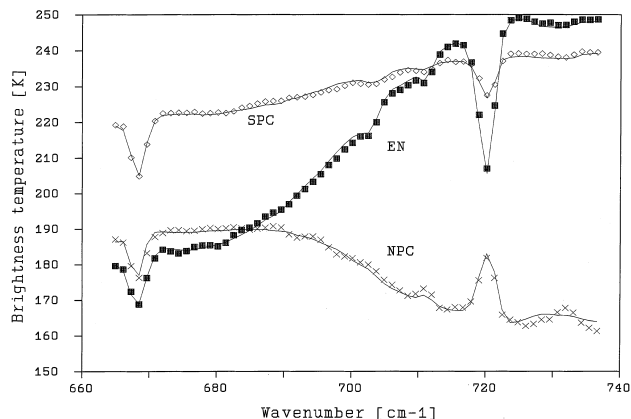
Fig. 17. Comparison of measured (symbols) and simulated (solid lines) IRIS spectra in the 15 μm CO_2 band. Notations see Fig. 16.
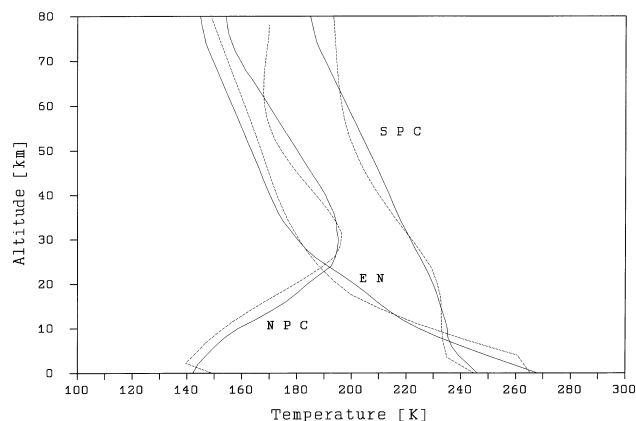

Fig. 18. Results of temperature retrieval from IRIS measurements. Notations see Fig. 16. Solid lines: Smith method, dotted lines: Tikhonov method.

respectively. The EN and SPC measurements show a weak aerosol band around 9.5 μm. Fig. 17 compares the resulting brightness temperatures (symbols) with simulated spectra (solid lines) in the right-hand wing (in the wavenumber picture) of the 15 μm CO_2 band. There is a rather good agreement between measurement and simulation indicating that the radiative transfer simulation algorithm works well. Deviations mainly occur in the spectra of the north polar cap and are due to low temperatures and the resulting smaller signal-to-noise ratio of the measurement. Noise features do also occur in the two other spectra. The retrieved temperature profiles using both Smith and Tikhonov method are shown in Fig. 18. The retrievals do not consider the appropriate aerosol amount in the above IRIS spectra (see Section 5.2). This will be done in the next future together with a clarification of differences. They are probably due to a different handling of measurement errors (noise).

5.2. Determination of aerosol optical depths at 9.5 μm

Analysing a defined measurement in the long-wavelength channel (LWC) and assuming a surface emissivity near 1.0 (which is close to reality) it will become clear at which position in the spectrum an aerosol band maximum (or minimum) occurs and which material-dependent spectral characteristic might be responsible for this signature. The corresponding ("nearest-by") substrate can then be selected from a range of synthetic aerosol spectra. This assumption is rather crucial and has to be used with great caution. The observed dust signatures in real Martian spectra reflect a mixture of many mineral compounds. The optical constants of such mixtures are not known and data on single terrestrial analog materials must be used as well as certain models on particle size distribution (see Section 3).

In Section 4.1 (Fig. 9), it was shown that a conservative scattering model is able to produce reasonable synthetic spectra in the thermal region. Thus, the determination of an equivalent absorbing opacity in that position in the spectrum where the maximum aerosol influence occurs and the use of an appropriate model substrate to obtain the optical depth as a function of wavenumber is regarded as an initial approximation that is not too bad in the region above 7 μm and especially at 15 μm where the temperature is extracted from.

The retrieval procedure that is tested till now uses the optical constants of palagonite and montmorillonite and a modified gamma size distribution function with a mean mode radius of 0.4 μm. Total aerosol optical depths (column depths) are determined by a least-squares fit (LSF) technique. The first aerosol iteration step is based on the temperature profile which has been retrieved from the 15 μm band without taking into account atmospheric aerosols. It considers a broad range of aerosol depths between 0.0 and 2.0. The resulting optical depths u^A can be far away from reality due to the strong temperature dependence of the spectra in the 9.5 μm region. The next step starts with a re-calculation of the 15 μm temperature profile considering the aerosol depth from the first step. The new profile is then used in the LSF to determine u^A again and so on. In this way, several iterations are performed moving from the 15 to the 9.5 μm region and back until convergence is achieved. The corrected temperature profile allows the use of a very fine grid of optical depths during higher iterations.

Fig. 19 shows the simulated spectra in comparison with measurements after four iterations when a simultaneous retrieval of temperature profile and aerosol optical depth is performed. The two lower curves are based on the simulated measurement MA3 with u^A (1050 cm^{-1}) = 1.0 while the two upper curves are valid for the IRIS measurement EN. An artificial noise was added to the MA3 spectrum which corresponds to the expected PFS noise level (0.4 mW/(m^2 sr cm^{-1}) near 670 cm^{-1} with increasing tendency above 1200 cm^{-1}. The IRIS signatures
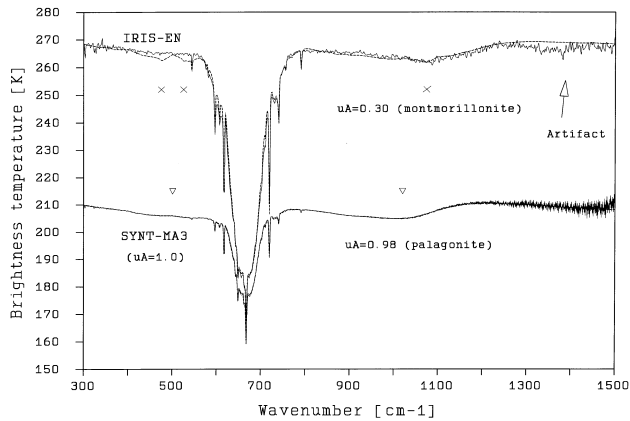
Fig. 19. Comparison of measurement (solid lines) and simulation (dashed lines) when simultaneous temperature profile and aerosol optical depth retrievals are performed. Upper curves: IRIS-EN (symbols x: montmorillonite features), lower curves: synthetic measurement MA3 (symbols ∇: palagonite features).

Fig. 20. Synthetic spectra of Mars as a function of surface pressure in the 2.0 μm CO_2 band. Top to bottom: $p_s = 1, 3, 6, 9$ mb.

around 1350 cm^{-1} are probably due to instrumental artifacts. The aerosol LSF procedure determines optical depths of 0.98 and 0.30 for the MA3 and EN spectra, respectively. The MA3 fit is in excellent agreement with the simulated measurement for both temperature and aerosol depth indicating that the retrieval procedures work well. A better fit of IRIS measurements around 9 μm was obtained using montmorillonite microphysical parameters instead of palagonite parameters which are the basis for creating synthetic measurements. But the IRIS measurements do not show the typical montmorillonite features at 20 μm (crosses in the figure). This indicates again that reality has to be described by using mixtures of different minerals.

5.3. Determination of surface pressure at 2.0 μm

Contrary to the thermal region, the spectra in the solar region are characterized by a small temperature dependence. But there is a strong dependence on surface pressure. Fig. 20 describes this behaviour in the central part of 2.0 μm CO_2 band which is very sensitive to pressure variations due to the fact that the total transmittance of the atmosphere is far from zero, i.e. the 2.0 μm band is unsaturated. While the band wing around 5017 cm^{-1} is only little influenced by pressure variations, the centre radiance (e.g. at 4987 cm^{-1}) significantly decreases with increasing pressure due to stronger absorption.

It is clear from Figs. 11 and 12 that the observed radiances strongly depend on the surface reflectance A_s and aerosol optical depth u^A and a simultaneous retrieval of p_s, A_s and u^A is necessary to obtain reliable results. Contrary to the high spectral variability due to pressure changes, the surface reflectance does not exhibit strong spectral signatures over the narrow interval of 30 cm^{-1}
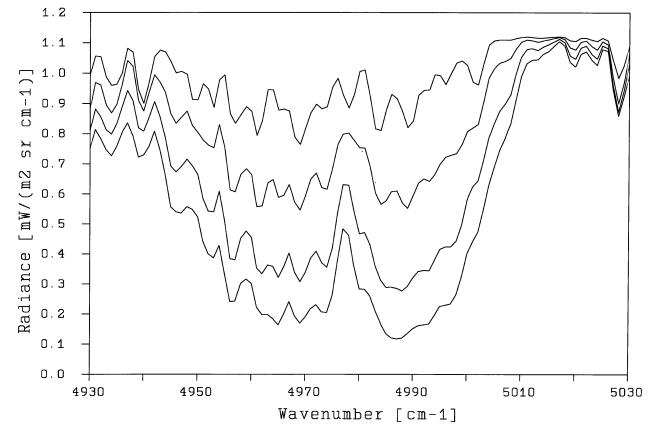
between band centre and wing. When the spectral variable A_s model of palagonitic soils (Arnold et al., 1995, see Fig. 3) is used, a constant value of 0.21 can be applied in that region. Provided the aerosol optical depth u^A is known, it is easy to retrieve surface pressure p_s and reflectance A_s simultaneously from LSF's comparing the radiance ratios at 5017 cm^{-1} (wing) and 4987 cm^{-1} (centre) for measurement and several on-line simulations.

The 2.0 μm retrieval procedure uses input data obtained from a preceding temperature profile and aerosol depth retrieval in the 15 and 9.5 μm bands, respectively. It is based on the assumption that the aerosol parameters (composition, size distribution, mode radius) used to calculate optical depths at 9.5 μm are adequate to characterize the 2.0 μm features. This assumption is again quite critical. Assuming incorrect parameters will have bad consequences in the SWC retrievals since one cannot ignore scattering in this part of the spectrum. Consequently, the choice of the right aerosol microphysical parameters is of greater importance than it is in the LWC region.

On the other hand, the 2.7 μm CO_2 band can be used to derive aerosol opacities as it is described in Section 5.4. This band is not too far away from 2.0 μm and the optical depths derived at 2.7 μm are probably close to 2.0 μm values (for basaltic dust they are). An alternating retrieval at 2.0 and 2.7 μm should help to find reasonable results.

5.4. Determination of aerosol optical depths at 2.7 μm

In Section 4.2 (Figs. 11 and 12), it was shown that atmospheric aerosols and surface reflectance features are able to produce similar spectral signatures in the solar region. But there is at least one region in the spectrum where the separation of influences due to aerosol optical depth u^A or reflectance A_s is possible. Fig. 21 shows simulated radiances ($A_s = 0.4$, $p_s = 6$ mb) in the 2.7 μm CO_2 band (3500–3800 cm^{-1}) for spectral constant optical depths of $u^A = 0.0, 0.1, 0.3, 0.5, 1.0$ and 2.0. Aerosol microphysical
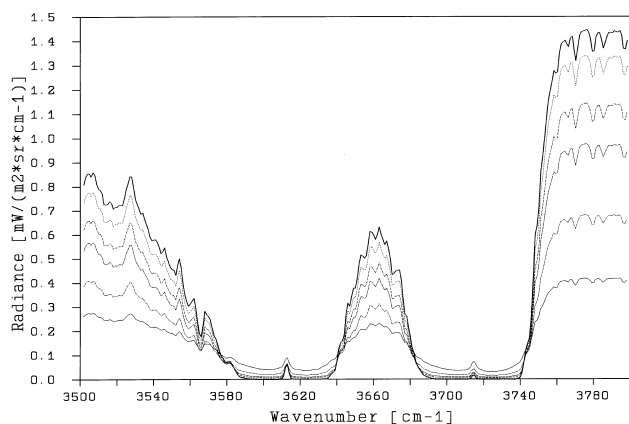
Fig. 21. Synthetic spectra of Mars as a function of aerosol optical depth in the 2.7 μm CO_2 band. Top to bottom in the vicinity of band centres: $u^A = 2.0, 1.0, 0.5, 0.3, 0.1$. The thick solid line shows the result for the dust-free atmosphere. $A_s = 0.4, \omega_0 = 0.70, g = 0.64$.
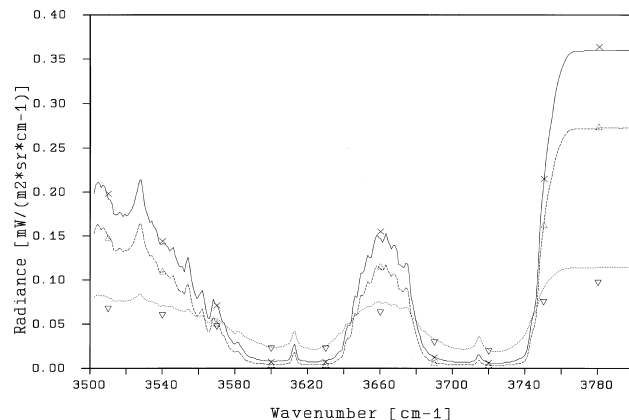

Fig. 22. Comparison of synthetic spectra in the 2.7 μm CO_2 band obtained with different multiple scattering codes. Lines: SA, symbols: SHDOM. $A_s = 0.1, g = 0.65$. Solid line: $u^A = 0.3$ (at 2.7 μm), $\omega_0 = 0.9$, dashed line: $u^A = 0.3, \omega_0 = 0.5$, dotted line: $u^A = 2.0, \omega_0 = 0.5$.

parameters used in this simulation are $\omega_0 = 0.70$ and $g = 0.64$. It is evident that the saturated 2.7 μm band exhibits a remarkable feature compared with other spectral regions. In its centre region, the radiance increases continuously with increasing aerosol optical depth and the band becomes smoother. This behaviour allows a retrieval of total aerosol depths at known surface pressure (which can be determined in the 2.0 μm band as it was shown in Section 5.3) since the centre radiation is not influenced by surface radiation and, thus, is independent on A_s. A separate paper describes the aerosol retrieval in the 2.7 μm region in more detail (Titov et al., 2000). It is pointed out in that paper that PFS will obtain about 80 spectral points in the bottom of the 2.7 μm band. The expected NESR is about 0.004 mW/(m² sr cm^{-1}) in this region. PFS will give the opportunity to monitor aerosol optical depths with a precision better than 0.1, therefore. Once the aerosol depth is retrieved, the surface reflectance in that spectral region can be derived from LSF's outside the band. As it is done in the thermal spectral region, repeated iterations within two different regions (2.0 and 2.7 μm here) and several switches between them allow to enhance the overall accuracy of retrieved parameters.

Fig. 22 shows a comparison of successive approximation (SA) and spherical harmonics discrete ordinate method (SHDOM), Evans, 1998) results for 3 pairs of data for aerosol depth u^A and ω_0 (solid line: 0.3/0.9, dashed line: 0.3/0.5, dotted line: 2.0/0.5). H_2O influence which mainly occurs at the right-hand band flank was neglected in these simulations. At small and moderate optical depths, the agreement between both methods is very good. The SA method produces somewhat larger radiances in the wings at large optical depths (dotted curve). Compared with SHDOM, the u^A retrieval yields approximately the same results, but the A_s retrieval would result in larger values at a high dust loading of the atmosphere.
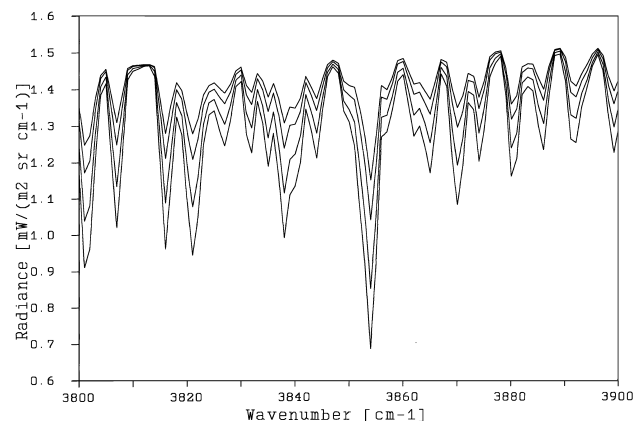
Fig. 23. Synthetic spectra of Mars as a function of H_2O mixing ratio in the 2.7 μm CO_2 band. Top to bottom: 100, 200, 500, 1000 ppm.

5.5. Determination of minor constituent column depths

The general view of the Martian pure gaseous near-infrared spectrum is described in Fig. 11. The detailed appearance of the clear atmosphere radiance spectrum in the 2.6 μm water vapour band is shown in Fig. 23 using the NOM model and $A_s = 0.3$. These spectra were calculated for four altitude-independent H_2O mixing ratios 100, 200, 500, and 1000 ppm, respectively. There is a high variability in the spectra with maximum differences around the line centres (e.g. at 3853 cm^{-1}). On the other hand, line wing regions (e.g. at 3812 or 3876 cm^{-1}) are little influenced. The determination of column optical depths and corresponding abundances can be performed applying again a LSF procedure.

Table 1
A possible sequence of retrieval steps including LWC and SWC measurements

Step	Paramter	Spectral region	Aerosol
1	T_s	LWC, signature-dependent, palagonite H2: 8 μm, 42 μm	No
2	$T(z)$	LWC, 15 μm	No
3	u_{LW}^{Aer}	LWC, signature-dependent, palagonite H2: 9.5 μm — cycle	Yes
4	$T(z)$	LWC, 15 μm —	Yes
5	p_s, A_s	SWC, 2.0 μm — cycle	Yes
6	u_{sw}^{Aer}, A_s	SWC, 2.7 μm —	Yes
7	$T(z)$, u_{LW}^{Aer}	LWC, 15 μm + aerosol region	Yes
8	$Q_{H_2O}(z)$, $Q_{CO}(z)$	LWC, SWC: 40/1.9, 2.6 μm, SWC: 4.7 μm, 2.4 μm	Yes
9	$u^{Aer}(z)$, $f(r)$	LWC: 8–13 μm, SWC: 2–3 μm	Yes

5.6. A proposed retrieval scheme and discussion of uncertainties

The complete retrieval program for all spectral regions including LWC and SWC measurements will run several times until convergence is obtained for the full set of atmospheric and surface parameters. A possible sequence is described in Table 1.

The surface temperature T_s is determined at first directly from the measurement data in a spectral region outside the atmospheric absorption bands followed by the temperature profile $T(z)$ retrieval using the 15 μm CO_2 band signatures. These two steps do not consider aerosols suspended in the atmosphere. The initial surface pressure p_s is obtained from terrain models. Step 3 yields a first estimate of aerosol opacity u^A in the region of maximum aerosol influence. This value is scaled with wavenumber according to model assumptions on aerosol microphysical parameters to determine optical depths at 15 μm. Steps 2 is repeated considering the dust opacity now (step 4). Steps 3 and 4 will cycle until convergence in the determination of $T(z)$ and u^A is achieved. The cycle over steps 5 and 6 performs the retrieval of surface pressure p_s, surface reflectance A_s and aerosol opacity u^A at 2.7 μm. Using the new pressure value p_s, the temperature and LW aerosol retrieval can be repeated (step 7) and so on. Future investigations (steps 8 and 9) will try to extract information on vertical density profiles of gaseous and particulate species from the measurement data.

The quantification of possible errors is a difficult task and final estimates cannot be given at the moment. Fig. 14a and b show that the retrieved temperature profiles are in good shape compared with the basis profiles. A total number of 47 synthetic spectra has been investigated in the thermal infrared with most of them containing pre-defined aerosol signatures. Maximum deviations between retrieved and basis profiles do rarely exceed 3 K below 50 km since a simultaneous retrieval of temperature profile and aerosol optical depth is performed. The average error of dust opacities determined at 9.5 μm is 0.03. In some cases, deviations around 0.1 occurred for optical depths of 1.0 or higher. As it was discussed in Section 5.1, neglect of dust opacity can lead to temperature errors up to 10 K near the surface. Uncertainties in surface pressure cause a shift of temperature profiles along the altitude axis.

The spectra in the solar region are characterized by a small temperature dependence. This is the reason why uncertainties in the temperature profile up to 15 K are of minor importance for pressure and aerosol retrievals in the PFS-SWC region. Five examples were tested where the temperature profile was shifted by 10 K, but the maximum pressure error determined at 2.0 μm did not exceed 5%. The problem which may arise in the SWC retrievals is due to the aerosol. Assuming an incorrect material (i.e. wrong microphysical parameters like single scattering albedo or particle size distribution) can result in wrong surface pressure values (which strongly depend on aerosol characteristics). As it is indicated in Table 1, a cycling retrieval in the 2.0 and 2.7 μm bands will probably minimize the p_s and u^A errors. Provided the micro-physical parameters of dust are at least approximately known the average relative errors of pressure and aerosol opacity retrieval were found to be below 3% (average over 47 synthetic spectra). When large optical depths are used at 2.0 μm that are wrong by a factor of 2 the resulting maximum pressure error Δp_s is about 15% and this wrong pressure leads to a uncertainty of 2.7 μm opacity Δu^A of about 20%. When the surface reflectance A_s was fixed during the experiment, $\Delta u^A = 6\%$ was found. These estimates are only valid for the special conditions tested.

6. Summary

A radiative transfer simulation and retrieval technique (RRT) was described which is used to calculate radiances and brightness temperatures at the top of the Martian atmosphere considering absorption, emission and multiple scattering by molecular (CO_2, H_2O, CO) and particulate (montmorillonite, palagonite) species. These synthetic infrared spectra were used for simultaneous retrievals of atmospheric and surface properties (vertical temperature profiles, surface temperature and pressure, surface

Table 2
Main parameters of previous and planned FTIR spectrometers in planetary missions (after Hirsch et al., 1996; PFS parameters updated)[a]

Instrument	IRIS-M	IRIS-V	FS-1/4	TES	CIRS	PFS
Planet	Mars	Jupiter, Saturn, Uranus, Neptune	Venus	Mars	Saturn, Titan	Mars
Spacecraft	Mariner 9	Voyager 1,2	Venera15/16	MO, MGS	Cassini	ME
DOL	1971	1978	1983	1992, 1996	1997	2003
SRA (μm)	5–50	4–55	6–40	6–60	7–16, 16–1000	1.25–5, 6–45
SRES (cm^{-1})	2.5	4.3	5	5–10	0.5–20	2
Beamsplitter	CsI	CsI	CsI	CsI	KCl, polarizers	CaF_2, CsI
FOV (deg)	4.5	0.25	4×4	0.5×0.5	MIR: 0.015×0.015 FIR: 0.25	SWC: 2, LWC: 4
NESR ($mW/(m^2\,sr\,cm^{-1})$)	0.5	0.1	0.2	0.15	0.0032, 0.02	0.004, 0.2
T/I (s)	18	46	5.5	6	50–2.5	4
AS, DF	No	No	No	Yes, 1	Yes, 1	Yes, 1
OB-FFT	No	No	Yes	Yes	No	Yes
TM (kg)	15	18	30	14.4	32	33.4
MPC (W)	20	14	30	12.5	29	35

[a] IRIS: Infrared Interferometric Spectometer, FS: Fourier Spectrometer, TES: Thermal Emission Spectrometer, CIRS: Composite Infrared Spectrometer, PFS: Planetary Fourier Spectrometer, MO: Mars Observer, MGS: Mars Global Surveyor, ME: Mars Express, DOL: Date of launch, SRA: Spectral range, SRES: Spectral resolution, FOV: Field of view, NESR: Noise equivalent spectral radiance, T/I: Time per interferogram, AS: Angle scanning, DF: Degrees of freedom, OB-FFT: Onboard fast Fourier transformation, TM: Total mass, MPC: Mean power consumption, MIR: Mid infrared, FIR: Far infrared, SWC: short wavelength channel, LWC: long wavelength channel.

Table 3
Observing strategy of PFS

Nominal height H_p of pericentre (km)	250
Spatial resolution at H_p on surface (km)	LWC: 8.7, SWC: 17.5
Major elliptical axis (km)	14980
Inclination (deg)	86.35
Orbital period (h)	7.6 (6.7 after 440 days)
Mission lifetime	2 Mars years
Limb observations	Yes
Emission angle studies	Yes

reflectance and atmospheric aerosol optical depths). Temperature profiles and aerosol depths were also inverted from real (IRIS) measurements. The proposed retrieval scheme considers several atmospheric absorption bands in different parts of the thermal and solar spectral region between 200 and 8000 cm^{-1} (1.25–50 μm).

The Smith and Tikhonov retrieval techniques produce similar results of temperature profiles up to 50 km altitude. The influence of aerosol multiple scattering is well described by the successive approximation (SA) method as compared with discrete ordinate techniques SHDOM and DISORD.

Multiple scattering in the thermal region can be approximated by a conservative scattering mode that reduces the spectra processing time considerably.

Extinction effects due to the presence of atmospheric aerosols and soil reflectance features are separable in the spectral region of the 2.0 and 2.7 μm CO_2 bands.

Sources of uncertainties in different steps of the radiative transfer simulation and retrieval technique (RRT) were discussed. Some aspects have been identified where improvements are necessary, e.g. inclusion of H_2O and CO_2 ice clouds and consideration of surface emissivity variations in the thermal infrared. Future measurements performed in the Martian environment as well as in the laboratory are very important to reduce the large uncertainties in the microphysical parameters being representative for aerosols and clouds in the atmosphere of Mars.

Appendix A.

Table 2 shows a comparison of main parameters of previous and planned FTIR spectrometers in planetary missions.

Table 3 contains additional information about the observing strategy of PFS.

References

Arnold, G., Bishop, J.L., Schade, U., 1995. Ellipsometry, reflectance and emittance spectroscopy of quartz particle size separates, palagonitic soils and montmorillonite. Implications for remote sensing of planetary surfaces. Lunar Planet. Sci. 27, 41–42.

Blecka, M.I., Blanco, A., Fonti, S., Muci, A.M., Orofino, V., 1997. Modelling the influence of surface emittance and atmospheric transmittance on Martian spectra. Adv. Space Res. 19, 1281–1284.

Chahine, M.T., 1968. Determination of temperature profile in an atmosphere from its outgoing radiance. J. Opt. Soc. Am. 58, 1634–1637.

Chahine, M.T., 1970. Inverse problems in radiative transfer: determination of atmospheric parameters. J. Atmos. Sci. 27, 960–967.

Chahine, M.T., 1972. A general relaxation method for inverse solution of the full radiative transfer equation. J. Atmos. Sci. 29, 741–747.

Chassefiè re, E., Drossart, P., Korablev, O., 1995. Post-Phobos model of the altitude and size distribution of dust in the low Martian atmosphere. J. Geophys. Res. 100, 5525–5539.

Christensen, P.R., Anderson, D.L., Chase, S.C., Clancy, R.T., Clark, R.N., Conrath, B.J., Kieffer, H.H., Kuzmin, R.O., Malin, M.C., Pearl, J.C., Roush, T.L., Smith, M.D., 1998. Results from the Mars global surveyor thermal emission spectrometer. Science 279, 1692–1698.

Drossart, P., Rosenquist, J., Erard, S., Langevin, Y., Bibring, J.P., Combes, M., 1991. Martian aerosol properties from the Phobos/ISM experiment. Ann. Geophys. 9, 754–760.

Evans, K.F., 1998. The spherical harmonics discrete ordinate method for three-dimensional atmospheric radiative transfer. J. Atmos. Sci. 55, 429–446.

Evans, D.L., Adams, J.B., 1979. Comparison of Viking lander multispectral images and laboratory reflectance spectra of terrestrial samples. Lunar Planet. Sci. 10, 1829–1834.

Forget, F., 1998. Improved optical properties of the Martian atmospheric dust for radiative transfer calculations in the infrared. Geophys. Res. Lett. 25, 1105–1108.

Formisano, V., Moroz, V.I., Hirsch, H., Arnold, G., Driescher, H., 1996. Infrared spectrometer PFS for the Mars94 orbiter. Adv. Space Res. 17, 1261–1264.

Gerstl, S.A.W., Zardecki, A., 1985. Discrete-ordinates finit-element method for atmospheric radiative transfer and remote sensing. Appl. Opt. 24, 81–93.

Hanel, R.A., Conrath, B.J., Hovis, W.A., Kunde, V.G., Lowman, P.D., Pearl, J.C., Prabhakara, C.P., Schlachman, B., 1972a. Infrared spectroscopy experiment on the Mariner 9 mission: preliminary results. Science 175, 305–308.

Hanel, R.A., Conrath, B.J., Hovis, W.A., Kunde, V.G., Lowman, P.D., Maguire, W.C., Pearl, J.C., Pirraglia, J., Prabhakara, C.P., Schlachman, B., Levin, G., Straat, P., Burke, T., 1972b. Investigation of the Martian environment by infrared spectroscopy on Mariner 9. Icarus 17, 423–442.

Hansen, J.E., Travis, L.D., 1974. Light scattering in planetary atmospheres. Space Sci. Rev. 16, 527–610.

Haus, R., 1995. Influence of aerosols and clouds on tropospheric infrared radiative transfer and air pollution remote sensing, In: Fabian, P., Klein, V., Tacke, M., Weber, K., Werner, Ch. (Eds.), Air Pollution and Visibility Measurements. Proc. SPIE Vol. 2506, pp. 564–575.

Haus, R., Goering, H., 1990. Radiative energy balance of the Venus mesoshere. Icarus 84, 62–82.

Haus, R., Schäfer, K., Bautzer, W., Heland, J., Mosebach, H., Bittner, H., Eisenmann, T., 1994. Mobile FTIS-monitoring of air pollution. Appl. Opt. 33, 5682–5689.

Haus, R., Wilkinson, R., Heland, J., Schäfer, K., 1998. Remote sensing of gas emissions on natural gas flares. Pure and Appl. Opt. 7, 853–862.

Hirsch, H., Formisano, V., Moroz, V.I., Arnold, G., Jurewicz, A., Michel, G., Lopez-Moreno, J.J., Piconni, G., Cafaro, N., 1996. The planetary Fourier spectrometer PFS for the orbiter of the spacecraft Mars 96. Planet. Space Sci. 44, 889–897.

Irvine, W.M., 1975. Multiple scattering in planetary atmospheres. Icarus 25, 175–204.

Isaacs, R.G., Wang, W.C., Worsham, R.D., Goldenberg, S., 1987. Multiple scattering LOWTRAN and FASCODE models. Appl. Opt. 26, 1272–1281.

Johnson, D.L., James, B.F., Justus, C.G., Chimonas, G., 1989. The Mars global reference atmosphere model (MARSGRAM), NASA Marshall Space Flight Center Technical Report.

Kahn, R.A., Martin, T.Z., Zurek, R.W., Lee, S.W., 1992. The Martian dust cycle. In: Kieffer, H.H., Jakowsky, B.M., Snyder, C.W., Matthews, M.S. (Eds.), Mars. University of Arizona Press, Tucson & London, pp. 1017–1053.

Kieffer, H.H., 1976. Soil and surface temperatures at the Viking landing sites. Science 194, 1344–1346.

Lellouch, E., Clancy, T., Crisp, D., Kliore, A., Titov, D.V., Bougher, S.W., 1997. Monitoring of mesospheric structure and dynamics. In: Venus-2. pp 295–324.

Liou, K.N., 1973. A numerical experiment on Chandrasekhar's discrete-ordinate method for radiative transfer: applications to cloudy and hazy atmospheres. J. Atmos. Sci. 30, 1303–1326.

Martin, T.Z., 1986. Thermal infrared opacity of the Mars atmosphere. Icarus 66, 2–21.

Martin, T.Z., Kieffer, H.H., 1979. Thermal infrared properties of the Martian atmosphere: 2. The 15 μm band measurements. J. Geophys. Res. 84, 2843–2852.

Meador, W.E., Weaver, W.R., 1980. Two-stream approximations to radiative transfer in planetary atmospheres: a unified description of existing methods and a new improvement. J. Atmos. Sci. 37, 630–643.

Moroz, V.I., Izakov, M.N., Linkin, V.M., 1988. Engineering model of the atmosphere of Mars (Draft version MA-87). Academy of Sciences USSR, Space Research Institute, PR1449.

Ockert-Bell, M.E., Bell III, J.F., Pollack, J.B., McKay, C.P., Forget, F., 1997. Absorption and scattering properties of the Martian dust in the solar wavelengths. J. Geophys. Res. 102, 9039–9050.

Owen, T., 1992. The composition and early history of the atmosphere of Mars. In: Kieffer, H.H., Jakowsky, B.M., Snyder, C.W., Matthews, M.S. (Eds.), Mars. University of Arizona Press, Tucson & London, pp. 818–834.

Pollack, J.B., Colburn, D.S., Flasar, F.M., Kahn, R., Carlston, C.E., Pidek, D.C., 1979. Properties and effects of dust particles suspended in the Martian atmosphere. J. Geophys. Res. 84, 2929–2945.

Rothman, L.S., Rinsland, C.P., Goldman, A., Massie, S.T., Edwards, D.P., Flaud, J.M., Perrin, A., Camy-Peyret, C., Dana, V., Mandin, J.Y., Schröder, J., McCann, A., Gamache, R.R., Wattson, R.B., Yosino, K., Chance, K., Jucks, K., Brown, L.R., Nemtchinov, V., Varanasi, P., 1998. The 1996 HITRAN molecular spectroscopic database and HAWKS (HITRAN Atmospheric Workstation). J. Quant. Spectrosc. Radiat. Transfer 60, 665–710.

Roush, T., Pollack, J.B., Orenberg, J., 1991. Derivation of midinfrared (5-25 μm) optical constants of some silicates and palagonite. Icarus 94, 191–208.

Santee, M., Crisp, D., 1993. The thermal structure and dust loading of the Martian atmosphere during late southern summer: Mariner 9 revisited. J. Geophys. Res. 98, 3261–3279.

Schäfer, K., Haus, R., Goering, H., Dubois, R., 1995. Venus mesosphere radiative transfer simulations on the basis of Venera-15 FTIR experiment. Adv. Space Res. 15, 69–72.

Singer, R.B., 1982. Spectral evidence for the mineralogy of high albedo soils and dust on Mars. J. Geophys. Res. 87, 10,159–10,168.

Smith, W.L., 1970. Iterative solution of the radiative transfer equation for the temperature and absorbing gas profile of an atmosphere. Appl. Opt. 9, 1993–1999.

Snyder, C.W., Moroz, V.I., 1992. Spacecraft exploration of Mars. In: Kieffer, H.H., Jakowsky, B.M., Snyder, C.W., Matthews, M.S. (Eds.), Mars. University of Arizona Press, Tucson & London, pp. 71–119.

Sobolev, V.V., 1963. A Treatise on Radiative Transfer. D.Van Nostrand, New York.

Spänkuch, D., 1987. International comparison of transmittance and radiance algorithms (ITRA). Report of the Nadir Group, Main Meteorological Observatory, Potsdam, GDR.

Stamnes, K., Tsay, S.C., Wiscombe, W., Jayaweecra, K., 1988. Numerical stable algorithm for discrete-ordinate method of radiative transfer in multiple-scattering and emitting layered media. Appl. Opt. 27, 2502–2509.

Thekaekara, M.P., 1973. Solar energy outside the Earth's atmosphere. Sol. Energy 14, 109–127.

Tikhonov, A.N., Arsenin, V.Y., 1977. Solutions of ill-posed problems. Wiley, New York.

Titov, D.V., 1995. Radiative balance in the mesosphere of Venus from the Venera-15 infrared spectrometer results. Adv. Space Res. 15, 73–77.

Titov, D.V., Fedorova, A.A., Haus, R., 2000. A new method of remote sounding of the Martian aerosols by means of spectroscopy in the 2.7 μm CO_2 band. Planet. Space Sci. 48, 67–74.

Titov, D.V., Haus, R., 1997. A fast and accurate method of calculation of gaseous transmission functions in planetary atmospheres. Planet. Space Sci. 45, 369–377.

Titov, D.V., Haus, R., Schäfer, K., 1992. Thermal fluxes and cooling rates in the Venus atmosphere from Venera-15 infrared spectrometer data. Adv. Space Res. 12, 73–77.

Toon, O.B., Pollack, J.B., Sagan, C., 1977. Physical properties of the particles composing the Martian dust storm of 1971–1972. Icarus 30, 663–696.

Wiscombe, W.J., 1980. Improved Mie scattering algorithms. Appl. Opt. 19, 1505–1509.

Zasova, L.V., 1994. Structure of the middle atmosphere of Venus and its upper clouds. Bull. Am. Astron. Soc. 26 (3), 1145.

Zasova, L.V., 1995. The structure of the Venusian atmosphere at high latitudes. Adv. Space Res. 16, 89–98.

Zurek, R.W., Barnes, J.R., Haberle, R.M., Pollack, J.B., Tillman, J.E., Leovy, C.B., 1992. Dynamics of the atmosphere of Mars. In: Kieffer, H.H., Jakowsky, B.M., Snyder, C.W., Matthews, M.S. (Eds.), Mars. University of Arizona Press, Tucson & London, pp. 835–933.